Preprint typeset using LaTeX style emulateapj v. 5/2/11

TESTING THE ORIGIN OF HIGH-ENERGY COSMIC RAYS

A. E. VLADIMIROV[1], G. JÓHANNESSON[2], I. V. MOSKALENKO[1,3], AND T. A. PORTER[1]

ABSTRACT

Recent accurate measurements of cosmic-ray (CR) protons and nuclei by ATIC-2, CREAM, and PAMELA reveal: a) unexpected spectral hardening in the spectra of CR species above a few hundred GeV per nucleon, b) a harder spectrum of He compared to protons, and c) softening of the CR spectra just below the break energy. These newly-discovered features may offer a clue to the origin of the observed high-energy Galactic CRs. We discuss possible interpretations of these spectral features and make predictions for the secondary CR fluxes and secondary to primary ratios, anisotropy of CRs, and diffuse Galactic γ-ray emission in different phenomenological scenarios. Our predictions can be tested by currently running or near-future high-energy astrophysics experiments.

Subject headings: astroparticle physics — diffusion — elementary particles — cosmic rays — ISM: general — dark matter — diffuse radiation — gamma rays: ISM — infrared: ISM — radio continuum: ISM — X-rays: ISM

1. INTRODUCTION

The spectrum of cosmic rays (CRs) has offered few clues to its origin so far. The only features observed are at very high and ultrahigh energies (see, e.g., Figure 1 in Swordy 2001): the so-called knee at a few times 10^{15} eV (Kulikov & Khristiansen 1958; Haungs et al. 2003), the second "knee" at $\sim 10^{18}$ eV, the "ankle" at higher energies (Abbasi et al. 2005), and a spectral steepening above 10^{20} eV (Abbasi et al. 2009; Abraham et al. 2010). Because of the limited size of Galactic accelerators and strength of magnetic fields in the acceleration region (e.g., in supernova remnants [SNRs]), it is believed that the CRs below the knee are Galactic, while above the knee they have an extragalactic origin, with the knee itself being due to propagation effects and a transition between the two populations of CRs (Berezinskii et al. 1990; Strong et al. 2007).

The power-law spectrum below the knee is thought to be the result of CR acceleration in SNR shocks (see, e.g., Drury et al. 2001), which is steepened to the observed index $\sim$ 2.75 by propagation in the interstellar medium (ISM) and eventual leakage from the Galaxy. The interstellar diffusion coefficient is typically assumed to be a power law in particle rigidity, based on numerous studies of magnetohydrodynamical turbulence (see, e.g., Biskamp 2003). The turbulent cascade often leads to a distribution of magnetic energy that is well described by a power law. For energies below $\sim$ 20 GeV nucleon^{-1}, the CR spectrum flattens due to the modulation in the heliosphere — a combined effect of the solar wind and heliospheric magnetic field. Measurements of CR composition below a few GeV nucleon^{-1} offer detailed information on elemental and isotopic abundances (Engelmann et al. 1990; Wiedenbeck et al. 2001; Obermeier et al. 2011), including the peaked shape of the secondary-to-primary nuclei ratio (e.g., B/C, sub-Fe/Fe) and abundances of long-lived radionuclides (such as ^{10}Be, ^{26}Al, ^{36}Cl, and ^{54}Mn). These measurements are used to derive the (model-dependent) diffusion coefficient and the size of the Galactic volume filled with CRs (Strong & Moskalenko 1998; Ptuskin & Soutoul 1998; Webber & Soutoul 1998), the so-called halo. Models of CR propagation are in reasonable agreement with available data (e.g., Strong et al. 2007; Trotta et al. 2011), with a few exceptions, including the unexpected rise in the positron fraction observed by PAMELA (Adriani et al. 2009).

The data recently collected by three experiments, ATIC-2 (Wefel et al. 2008; Panov et al. 2009), CREAM (Ahn et al. 2010; Yoon et al. 2011), and PAMELA (Adriani et al. 2011), indicate a break (hardening) of the spectra of the most abundant CR species above a rigidity of a few hundred GV. The break rigidity, $\rho_{\rm br}$, is best measured by PAMELA and occurs at approximately the same rigidity for p and He, $\rho_{\rm br} = 240$ GV. The PAMELA data for 10 GV $\lesssim \rho < \rho_{\rm br}$ agree very well with the earlier data from AMS and BESS (see Alcaraz et al. 2000; Haino et al. 2004 and Figure 1 of Adriani et al. 2011), while ATIC-2 data points for $\rho < \rho_{\rm br}$ are somewhat lower. We take the PAMELA data as the most accurate for $\rho < \rho_{\rm br}$. For $\rho > \rho_{\rm br}$, ATIC-2 results agree well with those of CREAM. The change in the spectral index (below/above the break) is estimated as $\Delta_{\rm br} = \gamma(> \rho_{\rm br}) - \gamma(< \rho_{\rm br}) = 0.15$, and is the same for protons and He.

Another important feature of the CR spectra discovered by these experiments is the difference between the spectral indices of CR protons and He. This has been speculated for a long time (e.g., Biermann et al. 1995, and references therein), but the experimental uncertainties were too large to be conclusive (see the collection of CR proton and He measurements in Moskalenko et al. 2002). The new measurements by the ATIC-2, CREAM, and PAMELA experiments confirm this with high significance. The spectrum of He is found to be harder than the spectrum of protons for energies up to, at least, 10^4 GV nucleon^{-1}. The difference between the proton and He spectral indices calculated by Adriani et al. (2011) using the PAMELA data is $\Delta\gamma = 0.10$, and it is approximately the same above and below $\rho_{\rm br}$. Within the statistical and systematic uncertainty, the measured p/He flux ratio appears to be a smooth function of rigidity, continuous at $\rho_{\rm br}$. This shows that the difference in the spectral slope of protons and He nuclei persists into the ultra-relativistic regime.

[1] W. W. Hansen Experimental Physics Laboratory Stanford University, Stanford, CA 94305, USA
[2] Science Institute, University of Iceland, Dunhaga 5, IS-107 Reykjavík, Iceland
[3] Kavli Institute for Particle Astrophysics and Cosmology, Stanford University, Stanford, CA 94305, USA

There is also fine structure in the spectra that may provide some clues to the nature of the observed features: PAMELA data clearly show a spectral softening at the break rigidity (which we refer to as the "dip", below). Adriani et al. (2011) have shown the softening to be statistically significant at the 95% confidence level for the spectra as functions of particle rigidity, and at the 99.7% level for the same data in terms of kinetic energy per nucleon. The softening is more pronounced in the He spectrum.

Rather than proposing a detailed interpretation of the observed features, in this paper we discuss broad categories of models, hereafter called *Scenarios*, and propose their observational tests. A particular realization of each scenario is called *Calculation*. The quantitative analysis is done using the GALPROP code[4] (Strong & Moskalenko 1998).

We study the interpretations of the p/He ratio variation separately from the interpretations of the spectral break at $\rho_{\rm br}$. In Section 2.1, we introduce the reference scenario based on the pre-PAMELA data. In Section 2.2, we discuss possible explanations of the p/He ratio decline with energy: inherent nature of CR sources and spallation effects. Section 2.3 presents four physical scenarios that could lead to the observed spectral break at $\rho_{\rm br}$: injection effects, propagation effects, and local low- or high-energy CR source. The framework of our CR propagation calculations is described in Sections 3.1 and 3.2, and specific calculation setups in Section 3.3. The sections following that discuss our results and their implications to CR observations and CR propagation modeling.

2. SCENARIOS

2.1. *Reference Case*

Scenario R: Reference scenario. First, we introduce a reference case based on the pre-PAMELA data. In this scenario, the CR injection spectrum above 10 GV is a single power law up to the "knee" in the CR spectrum, with the same spectral index for all CR species. The rigidity dependence of the diffusion coefficient at high energies is also taken as a single power law for all energies. The CR source distribution is described in Section 3.

Scenario R provides reasonable agreement with the pre-PAMELA data, but it cannot reproduce the spectral features evident in the new data discussed in this paper: the difference between proton and He spectra, the spectral break, or the dip. Below, we describe several broad categories of models that encompass viable explanations for these new features. The comparison of predictions for these other models for quantities other than CR proton, He, and electron spectra with predictions of *Calculation R* qualitatively illustrates the significance of the difference between different scenarios.

2.2. *p/He Ratio: Acceleration and Spallation Hypotheses*

The confirmation of a significant difference between proton and He spectral indices poses a challenge for theories of CR acceleration and propagation. Whatever the physical cause of this difference in spectra may be, it seems to affect heavier nuclei in the same way as it does He (see, e.g., Ahn et al. 2009, for spectra of nuclei), giving them a harder spectrum than that of protons.

Diffusive shock acceleration (DSA) predicts the spectrum of He *trapped* in a shock to be harder than that of protons due to its lower Z/A ratio, but only for non-relativistic energies (e.g., Ellison et al. 1997). However, in particles *escaping* from a shock, p/He ratio may decline with energy, if DSA is rapid, and the injection of He into the acceleration process varies in a way that enhances He acceleration in young shocks. This could happen due to the inherent property of particle injection in shocks (Malkov et al. 2012), or if the abundance of He (Ohira & Ioka 2011) or magnetic field orientation (Biermann et al. 1995) is inhomogeneous in the SNR environment. We encompass these mechanisms into the Acceleration Hypothesis (*Hypothesis A*), which is discussed below. Note that propagation effects may contribute to the p/He spectral difference because the second-order Fermi process (reacceleration) in the interstellar medium makes the He spectrum harder due to its lower Z/A ratio. This effect, however, does not extend to the ultra-relativistic regime (e.g., Strong et al. 2007).

An alternative idea, suggested by Blasi & Amato (2012a), is that that spallation of CR nuclei ($Z > 1$) may lead to hardening of their spectra. This is because the lower energy CRs have longer confinement times in the Galaxy, and their flux is depleted by spallation more than the flux of higher energy nuclei. Hardening occurs only if the spallation timescale is short compared to the confinement timescale of the nuclei. Note that Blasi & Amato (2012a) consider CRs at energies above 1 TeV and do not attempt to make their model consistent with the CR data at low energies, where various effects, such as stochastic reacceleration and significant production of secondaries, come into play. We investigate this idea, extending it to lower energies, and hereafter refer to it as *Hypothesis S*. Our calculations include spallation of all nuclei species at all energies, the default with GALPROP. However, as our results for *Calculation R* show (see Section 4), the effect of spallation on the He spectrum is insignificant, and the p/He ratio above 10 GV is flat. Below, we demonstrate that, with some model tuning (i.e., *Calculation* $S_{1,2}$), fragmentation may indeed lead to hardening of the He spectrum. We also assess the consequences of the required model modifications.

Note that in this section we refer to the results of our calculations for *Hypothesis S*. The framework and details of these calculations are formally introduced later in the text in Section 3. However, we would like to briefly discuss *Hypothesis S* here, because in the rest of the paper we discard *Hypothesis S* and adopt the assumption that the p/He decline is caused by the nature of CR accelerators (*Hypothesis A*). The reader interested in our reasoning for discarding the spallation effects hypothesis may find the explanation in this section. And a detailed description of our physical model, computational method and data sources can be found in Sections 3 and 4, where we discuss the spectral break at $\rho_{\rm br}$.

Hypothesis S: Spallation effects. The fraction of fragmented CR nuclear species depends on their total inelastic cross section and the effective grammage encountered by the CR species in the Galaxy. Inelastic cross section fits used in Blasi & Amato (2012a), taken from Hörandel et al. (2007), are somewhat larger than those used in our calculations (Barashenkov 1993; Barashenkov & Polyanski 1994). Besides that, the gas number density used in calculations by Blasi & Amato (2012a) yields a significantly larger grammage than in our standard models. To segregate these effects, we construct two calculation setups for *Hypothesis S*: *Calculation* S_1 and *Calculation* S_2. Both calculations adopt the cross section fits from Hörandel et al. (2007). *Calculation S* uses parameters similar to that of the reference *Calculation R*,

[4] The project Web site http://galprop.stanford.edu/

but a slightly smaller diffusion coefficient to match the value used by Blasi & Amato (2012a). In *Calculation S_2*, we additionally increase the gas number density relative to *Calculation R* by a factor of two. Note that these calculations use the GALPROP code, which was adapted to incorporate the above-mentioned inelastic cross sections, whereas the production of fragments (daughter isotopes) is calculated using a standard set of cross sections and remains unchanged.

Our calculations show that with our standard gas distribution based on astronomical data (Moskalenko et al. 2002), *Calculation S_1*, the amount of hardening is insufficient to provide agreement with the PAMELA p/He ratio. The required hardening of the He ($^3\mathrm{He} + {}^4\mathrm{He}$) spectrum can be achieved only if we assume a considerable increase in grammage and simultaneously adopt a set of total inelastic cross sections from Hörandel et al. (2007), *Calculation S_2*. However, this leads to an overproduction of secondary species in CRs, such as antiprotons and boron, so that the calculated B/C ratio does not agree with the data. The p/He ratio obtained in *Calculation S_1* and *Calculation S_2* is shown in the top panels of Figure 7 (see Section 3.2 for an overview of the plain diffusion and diffusive-reacceleration models). The calculated B/C ratio and $\bar{p}$ flux are shown in the middle and bottom panels, respectively. Read on and see Figures 1–3 for details on the parameters of the calculations shown in Figure 7.

Another important point to consider here is that the measurements of PAMELA, ATIC-2, and CREAM are not sensitive to the isotopic composition of CR fluxes. The He fluxes reported by these experiments and used throughout this paper are, in fact, the sum of ^{3}He and ^{4}He species. The dominant channel of ^{4}He spallation is the reaction

$$^4\mathrm{He} + \mathrm{p} \rightarrow {}^3\mathrm{He} + \mathrm{X}.$$

This reaction leads to a hardening of the interstellar ^{4}He spectrum because lower energy nuclei experience more spallation events. However, due to production of ^{3}He in the same reaction, the *total* He spectrum does not harden as much as ^{4}He alone. Further spallation of secondary ^{3}He, as well as fragmentation of ^{4}He into products other than ^{3}He, eventually leads to the total He spectrum hardening. Still, the effect of spallation on the total He spectrum is not as strong as on ^{4}He alone. Equation (2.1) in Blasi & Amato (2012a) indicates that ^{3}He was not included in their calculations. Therefore, their results would be relevant only for the $p/^4$He ratio.

This is illustrated in Figure 7, where we also plot the ratio of $p/^4$He in *Calculation S_2* for reference. It can be seen that the overall shape of the $p/^4$He ratio matches the measured p/He ratio well; however, a significant fraction of secondary ^{3}He changes the shape so that the calculated p/He ratio cannot be adjusted to match the data simultaneously at all rigidities (1 GV – 10 TV).

Hypothesis A: Acceleration effects. We have concluded that the adjustments of propagation model required to reproduce the observed p/He ratio in *Hypothesis S_2* conflict with the measurements of secondary CR species. Therefore, in the rest of this work we adopt an alternative to *Hypothesis S*, which we call the "Acceleration hypotheses". *Hypothesis A* represents the idea that the nature of CR accelerators is responsible for a harder spectrum of He than p (see references at the beginning of this section). To incorporate *Hypothesis A* into our calculations, we use an ad hoc modification for the CR injection spectra. That is, our calculations assume that nuclei heavier than H are injected into the ISM with a harder spectrum than protons. The difference between the spectral indices of protons and heavier nuclei is the same for all rigidities and is $\Delta_{p/\mathrm{He}} = 0.07$.

We do not present a separate calculation for the *Hypothesis A* in this paper. Instead, we incorporate *Hypothesis A* into calculations that study scenarios *P, I, L* and *H* for the break in the p and He spectra (those scenarios are introduced in Section 2.3). Figure 5 shows the p/He ratio resulting from this modification (see below for parameters of other calculations shown in this figure). The figure illustrate that the data reported by PAMELA, ATIC-2, and CREAM can be reproduced by including $\Delta_{p/\mathrm{He}} = 0.07$.

2.3. *Spectral Break and Dip: Propagation, Injection and Local Source Scenarios*

We consider the following scenarios for an explanation of the break at ρ_{br} and the dip just below ρ_{br}: (1) interstellar propagation effects, (2) modification of CR injection spectrum at the sources, (3) composite Galactic CR spectrum, (4) effects of local sources at low energies ($\rho < \rho_{\mathrm{br}}$), and (5) effects of local sources at high energies ($\rho > \rho_{\mathrm{br}}$). Particular realizations of these scenarios (calculations) are discussed in detail in Section 3.3; their parameters are summarized in Tables 1 and 2.

Scenario P: interstellar Propagation effects. Transport of CRs in the ISM is subject to considerable uncertainties, because the properties of interstellar magnetic turbulence are not very well known (Elmegreen & Scalo 2004; Scalo & Elmegreen 2004). This makes CR observations a valuable indirect probe of quantitative features of particle transport (e.g., the diffusion coefficient, D) in the Galaxy. Therefore, in this scenario, the break in the observed proton and He spectra is attributed to a change in CR transport properties at rigidity ρ_{br}. This scenario is represented by *Calculation P*, which has a break in the rigidity dependence of the diffusion coefficient at $\rho = \rho_{\mathrm{br}}$. For $\rho < \rho_{\mathrm{br}}$, we use the functional form of $D(\rho)$ obtained in the earlier comprehensive analysis of CR data by Trotta et al. (2011), and for $\rho > \rho_{\mathrm{br}}$, we adjust the rigidity dependence of $D(\rho)$ to match the observations of PAMELA, ATIC-2, and CREAM, as discussed above.

Scenario I (a): CR Injection effects, source with a spectral break interpretation. Existing models of CR production by SNR shocks (e.g., Caprioli et al. 2010; Ptuskin et al. 2010) predict a smooth spectrum of CR particles injected by an SNR into the Galaxy. Such models usually consider a shock in a semi-infinite medium or assume spherical symmetry. The spectrum predicted by these models may gradually harden with energy between 10 GeV and 100 TeV, but not as rapidly as in the PAMELA data. Note that particle transport, magnetic turbulence generation, and nonlinear feedback of particles and magnetic fields on shock structure are not strictly constrained in these models. The spectrum of particles leaking from an SNR shock has never been observed directly. It is therefore conceivable that with some parameter tuning, present models of particle acceleration may predict a more pronounced hardening in the spectrum of particles injected into the ISM, consistent with the new data. Alternatively, particle acceleration models that take into account the asymmetry of SNRs may predict a break in the particle spectrum produced by a single SNR. For example, in the model of Biermann et al. (2010), the break, or upturn, occurs due to the contribution of the SNR's polar cap. This case, hereafter referred to as *Scenario I (a)*, is represented by *Calculation I*, which features a

Galaxy-wide source spectrum with a hardening at $\rho_{\rm br}$. The diffusion coefficient does not have a break in this scenario.

Scenario I (b)*: CR Injection effects, composite source interpretation*. While SNRs (isolated or in superbubble regions) are believed to be the primary sources of Galactic CRs, different classes of supernovae and their environments, as well as other CR sources, can combine to produce the observed CR spectrum. Generally speaking, different types of CR sources could have different spatial distributions throughout the Galaxy. In this work, we make the simplifying assumption (1) that there are only two types of CR sources, and (2) the spatial distributions are the same for both types of CR sources. If one source dominates the low energy part of the CR spectrum, and the other the high energy part, then *Calculation I*, with a hardening of the Galactic CR source at $\rho_{\rm br}$, adequately encompasses this composite source scenario as well. This scenario may be generalized to a distribution of CR sources with different parameters. Yuan et al. (2011) have shown that in general, dispersion in the CR source spectral indices results in the concavity of the observed CR spectrum. We use the same computational setup to calculate the observed quantities for *Scenario I* (a) and *Scenario I* (b), and we call it just *Calculation I*. A subtle advantage of the composite source interpretation of *Calculation I* (i.e., in *Scenario I* (b)) is its ability to explain the dip more naturally than the source with an inherent break scenario (see the discussion of the dip in Section 4).

Scenario L: local Low-energy source. This scenario encompasses interpretations that assume that the observed spectral break is caused by a local source dominating the CR spectrum at *low* rigidities, $\rho < \rho_{\rm br}$. Unlike *Scenario I* (b), the present scenario assumes that the low-energy source is not typical for the Galaxy as a whole. This scenario is formulated as *Calculation L*, in which the Galactic CR spectrum is hard, matching the observations of PAMELA, ATIC-2, and CREAM for $\rho > \rho_{\rm br}$. For $\rho < \rho_{\rm br}$, the flux of Galactic CRs is lower than the observed flux, and we assume that the difference is accounted for by the hypothetical local source. We assume the extreme case of a very local low energy source. This means that we do not calculate propagation of CRs from that source and only the Galactic sources with the hard spectrum are used to calculate the production of secondaries and the diffuse Galactic γ-ray emission. This scenario contrasts with *Scenario I* (b), where the sources of low-energy CRs are distributed across the Galaxy. The case of intermediate local source extent falls in between *Scenario L* and *Scenario I* (b).

Scenario H: local High-energy source. This scenario is analogous to *Scenario L*, but with Galactic sources dominating the CR flux for $\rho < \rho_{\rm br}$, and the spectral break produced by a local *high-energy* source dominating the observed flux for $\rho > \rho_{\rm br}$. The calculation representing this scenario is referred to as *Calculation H*. The assumption of the high-energy source being very local is made in this calculation identically to how it was done in *Calculation L*, i.e., the production of secondaries and the diffuse Galactic γ-ray emission is determined solely by the Galactic CR sources.

3. CALCULATIONS

3.1. *GALPROP Code*

The GALPROP project began in late 1990s (Strong & Moskalenko 1998) and has been in continuous development since. The code is available from the dedicated Web site where a facility for users to run the code via online forms in a web browser[5] is also provided (Vladimirov et al. 2011).

The GALPROP code solves the CR transport equation for a given source distribution and boundary conditions for all CR species. This equation includes diffusion, a galactic wind (convection), diffusive reacceleration in the ISM, energy losses, nuclear fragmentation, radioactive decay, and production of secondary particles and isotopes:

$$\frac{\partial\psi}{\partial t} = q(\mathbf{r},p) + \nabla\cdot(D_{xx}\nabla\psi - \mathbf{V}\psi) + \frac{\partial}{\partial p}p^2 D_{pp}\frac{\partial}{\partial p}\frac{1}{p^2}\psi - \frac{\partial}{\partial p}\left[\dot{p}\psi - \frac{p}{3}(\nabla\cdot\mathbf{V})\psi\right] - \frac{1}{\tau_f}\psi - \frac{1}{\tau_r}\psi\,, \quad (1)$$

where $\psi = \psi(\mathbf{r},p,t)$ is the CR number density per unit total particle momentum (i.e., $\psi(p)dp = 4\pi p^2 f(p)dp$ in terms of phase-space density $f(p)$), $q(\mathbf{r},p)$ is the source term, D_{xx} is the spatial diffusion coefficient, $\mathbf{V}$ is the convection velocity, reacceleration is described as diffusion in momentum space with diffusion coefficient D_{pp}, $\dot{p} \equiv dp/dt$ is the momentum loss rate, τ_f is the time scale for fragmentation, and τ_r is the timescale for radioactive decay. The numerical solution of the transport equation is based on a Crank-Nicholson (Press et al. 1992) implicit second-order scheme. The spatial boundary conditions assume free particle escape, e.g., $\psi(R_h,z,p) = \psi(R,\pm z_h,p) = 0$, where R_h and z_h are the boundaries for a cylindrically symmetric geometry.

The source function q is

$$q(\mathbf{r},\rho) = q_{\rm pri}(\mathbf{r},\rho) + \sum q_{\rm sec}(\mathbf{r},\rho), \quad (2)$$

where $q_{\rm pri}$ represents the primary CR sources, and the $q_{\rm sec}$ term is for the sources of secondary isotopes (i.e., nuclear reactions in the ISM), and $\rho \equiv pc/Ze$ is the magnetic rigidity where p is momentum and Ze is the charge. The distribution of primary Galactic CR sources used in this work is based on the supernova distribution from Case & Bhattacharya (1998).

While GALPROP's numerical scheme can accommodate arbitrary energy dependence of CR source function, in this work we parameterize the source function of primary nuclei as a broken power law in particle rigidity:

$$q_{\rm pri}(\mathbf{r},\rho) \propto Q(\mathbf{r})\left(\frac{\rho}{\rho_{\rm inj0}}\right)^g, \quad (3)$$

$$g = \begin{cases} g_0 \text{ for } \rho < \rho_{\rm inj0} \\ g_1 \text{ for } \rho_{\rm inj0} \le \rho < \rho_{\rm inj1} \\ g_2 \text{ for } \rho \ge \rho_{\rm inj1} \end{cases},$$

The source function for primary CR leptons is similar to that of nuclei, but with up to two breaks.

Likewise, the spatial diffusion coefficient is given by

$$D_{xx} = \beta D_0\left(\frac{\rho}{\rho_0}\right)^\delta, \quad (4)$$

$$\delta = \begin{cases} \delta_0 \text{ for } \rho < \rho_0 \\ \delta_1 \text{ for } \rho_0 \le \rho < \rho_1 \\ \delta_2 \text{ for } \rho \ge \rho_1 \end{cases},$$

where D_0 is the normalization at rigidity ρ_0 and $\beta \equiv v/c$. The power-law index $\delta = 1/3$ corresponds to Kolmogorov diffusion (see Section 3.1).

[5] http://galprop.stanford.edu/webrun/

GALPROP solves the time-dependent propagation equation, and in this work, the steady-state solutions of Equation (1) are obtained assuming that the source functions are time-independent and integrating the equation over a long enough time interval. The accelerated solution technique is used, where the initial time step, $\Delta t = 10^9$ yr, is large compared to the propagation timescale, and after $N_s = 20$ iterations, Δt is reduced by a factor of two, etc., until Δt becomes small compared to the shortest timescale in the system (in our case, 10 yr, to accommodate the rapid energy losses of leptons).

The details of physical processes and data used in the GALPROP code, as well as the numerical scheme, can be found elsewhere. A complete list of relevant publications is available in Vladimirov et al. (2011); the aforementioned GALPROP Web site contains additional information and publications.

3.2. *Diffusive-Reacceleration and Plain Diffusion Models*

Previous studies have shown that the available CR data can be explained in one of the two common propagation models: the *diffusive-reacceleration* (D-R) model and the *plain diffusion* (PD) model. These models have been used in a number of studies utilizing the GALPROP code (e.g., Moskalenko et al. 2002; Strong et al. 2004; Ptuskin et al. 2006b; Abdo et al. 2009, and references therein).

The D-R model assumes that low energy CRs in the ISM participate in the second-order Fermi acceleration process. This process is believed to be caused by stochastic collisions of CR particles with moving magnetic structures. Averaged in time, such collisions result in particle diffusion in momentum space with a diffusion coefficient D_{pp}, which increases the mean energy of low energy particles. If reacceleration is included, D_{pp} is related to D_{xx} (Berezinskii et al. 1990; Seo & Ptuskin 1994):

$$D_{pp}D_{xx} = \frac{4p^2 v_{\rm Alf}^2}{3\delta(4-\delta^2)(4-\delta)w}, \qquad (5)$$

where w characterizes the level of turbulence (we take $w = 1$ because only the quantity $v_{\rm Alf}^2/w$ is relevant), and $\delta = 1/3$ for a Kolmogorov spectrum of interstellar turbulence (Kolmogorov 1941) or $\delta = 1/2$ for a Kraichnan cascade (Iroshnikov 1964; Kraichnan 1965), but can also be arbitrary. Matching the B/C ratio below 1 GeV in D-R models is known to require large values of $v_{\rm Alf}$. In order to avoid a large bump in the proton spectrum at low energies, the D-R model requires a break in the CR injection function around $\rho = 10$ GV.

The PD model assumes no reacceleration process, which corresponds to $v_{\rm Alf} = 0$. No break in the CR injection function is required to fit the proton and helium spectra at low energies in the PD model. However, in order to fit the B/C data below 1 GeV nucleon^{-1}, the PD model requires a low-energy break in the diffusion coefficient. Specifically, the diffusion coefficient in the PD model must *decrease with increasing energy* below 4 GV in order to fit the B/C measurements below 1 GeV nucleon^{-1}. A possible physical justification of such behavior of $D(\rho)$ is given by Ptuskin et al. (2006c) and involves turbulence dissipation in the ISM.

Each of our calculations (*Calculation R*, *P*, *I*, *L*, and *H*) is presented in two versions: one for the D-R and another for the PD model.

3.3. *Calculation Setups*

The parameters of our calculations are summarized in Tables 1 and 2. Figures 1–3 show the diffusion coefficients and the injection spectra used for the different scenarios.

Calculation R is the reference case for this study. The list below outlines the key parameters of this calculation for the D-R and PD models.

1. For *Calculation R* in the D-R model, we chose $g_0 = -1.9$, $g_1 = g_2 = -2.4$ (i.e., no break at $\rho_{\rm inj1}$) and $\rho_{\rm inj0} = 11$ GV for all nucleons, which is consistent with the findings of Trotta et al. (2011) based on a Bayesian analysis of a D-R model using the GALPROP code. For the PD model, a low energy break in the injection spectrum is unnecessary, and our *Calculation R* uses $g_0 = g_1 = g_2 = -2.1$. The electron injection spectrum for *Calculation R* in the D-R model is similar to that from Ackermann et al. (2010), with spectral index in rigidity Γ=1.60/2.50 below/above a break rigidity of $\rho_{\rm e0}$=4 GV, and a second steepening to Γ=5.0 above $\rho_{\rm e2}$=2 TV. For the PD model, we use Γ=2.35 above 4 GeV. Note that the low-energy break in the electron injection function can be explained without the corresponding break in the proton injection spectrum, because electrons and protons may be accelerated in sources via different mechanisms.

2. For the diffusion coefficient, *Calculation R* uses $\delta = 0.30$ in the D-R model, and $\delta = 0.60$ in the PD model. The normalization for the diffusion coefficient in the D-R model is $D_0 = 5.75 \times 10^{28}$ cm s^{-1} at $\rho = 4$ GV, which is consistent with the best-fit values obtained by Trotta et al. (2011). For the PD model, we use $D_0 = 3.0 \times 10^{28}$ cm s^{-1}, in order to match the B/C observations of HEAO, TRACER, and CREAM (see Section 4.4). In this work, we construct the PD model with a constant, rather than decreasing, diffusion coefficient below 4 GV, even though the model does not reproduce the low energy B/C data. This is done in order to illustrate the possibility that a local low-energy CR source (*Scenario L*) can simultaneously explain the break in p, He spectra *and* fit the low-energy B/C data without requiring the diffusion coefficient to decrease with increasing energy (see below).

3. Finally, to model reacceleration in the D-R model, we chose $v_{\rm Alf} = 32$ km s^{-1}, the halo size $z_h = 4$ kpc, and the normalization of the propagated CR proton spectrum was tuned to the observed flux $N_p = 10.7 \times 10^{-12}$ cm^{-2} s^{-1} sr^{-1} MeV^{-1} for $\rho = 10^3$ GV. These values were obtained by slightly adjusting the best-fit values obtained by Trotta et al. (2011) to achieve a good agreement with the PAMELA proton spectrum for $\rho < \rho_{\rm inj0}$. These adjusted values are still within one mean square deviation of the posterior mean found by Trotta et al. (2011). In all figures, black lines represent the input and output quantities pertaining to *Calculation R*.

Calculation P has the same parameters as the reference *Calculation R*, except: (1) the injection spectrum of protons (electrons) above the low energy break $\rho_{\rm inj0}$ ($\rho_{\rm e0}$) has a softer power-law index to give agreement with the PAMELA data below $\rho_{\rm br}$; (2) the injection spectra of He and heavier elements ($A > 1$) have a power-law index harder than that of

protons by $\Delta_{p/\mathrm{He}}$ for all rigidities (this represents *Hypothesis A*); (3) the rigidity dependence of the diffusion coefficient, Equation (5), has a break at rigidity ρ_1 (i.e., $\delta_1 \neq \delta_2$). The break in the rigidity dependence of the diffusion coefficient is introduced to match the observed break in the CR spectrum. Besides, we choose $\rho_1 \approx \rho_{\mathrm{br}}$ so that ρ_1 is slightly larger than ρ_{br} for better agreement with the data for $\rho > \rho_{\mathrm{br}}$. The normalization of the proton flux has been adjusted in *Calculation P*, along with the abundance of He, to agree with PAMELA data at all energies (the abundances of heavier nuclei were changed by the same factor as He). The results for *Calculation P* are shown with blue lines in all figures.

Calculation I differs from *Calculation R* in the following ways: (1) the index of the proton injection spectrum is softer than in *Calculation R* for $\rho_{\mathrm{inj0}} < \rho < \rho_{\mathrm{inj1}}$; (2) the injection spectrum has two breaks, i.e., $g_1 \neq g_2$ (this represents *Scenario I* (a) and *Scenario I* (b)); (3) electrons also have a softer spectrum for $\rho_{\mathrm{e0}} < \rho < \rho_{\mathrm{e1}}$, and a break at ρ_{e1}, and (iv) nuclei are injected with a harder spectrum than protons (*Hypothesis A*). This calculation produces a CR spectrum at Earth with a break at ρ_{br} closely matching that of *Calculation P*, but due to a different physical assumption. Namely, it is the spectral break in the CR injection spectrum that produces the break in *Calculation I*, whereas in *Calculation P*, it occurs because of a break in the diffusion coefficient. Note that the high-energy break in the electron injection spectrum must be stronger than for protons, and it must occur at a lower rigidity than in protons, in order to obtain agreement with the electron spectra observed by the *Fermi*-LAT and PAMELA. The results of this calculation are shown as green lines.

Calculation H combines two components. One component is produced by the Galactic CR sources and propagated using GALPROP with the same parameters as *Calculation I*. This component does not have a break in the CR injection spectrum at ρ_{inj1} and its normalization was tuned to match the proton and He spectra for $\rho < \rho_{\mathrm{inj1}}$. Another component is produced by a hypothetical local source, which contributes to the total flux only for $\rho > \rho_{\mathrm{br}}$. We do not calculate CR propagation for the local source; instead, we calculate its spectrum at Earth by subtracting the Galactic source spectrum from the data of ATIC-2 and CREAM for $\rho > \rho_{\mathrm{br}}$. As discussed in Section 4, this represents the assumption that the local source is nearby and not very powerful. To compute secondary particles and isotopic ratios in this calculation, we assume that isotopic abundances in the local and Galactic sources are similar, and that the local source supplies no secondary particles at Earth. This lowers, for instance, the B/C and $\bar{p}/p$ ratios for $\rho > \rho_{\mathrm{br}}$. The diffuse γ-ray emission from the Galaxy is calculated using only CR fluxes from the Galactic source. Gray lines represent this calculation in plots.

Calculation L features a local source that contributes to the *low*-energy part of the CR spectrum ($\rho < \rho_{\mathrm{br}}$). The local source is included in the same way as in *Calculation H*, i.e., its propagated spectrum is calculated as the difference between the observed CR spectrum and the propagated Galactic component. As in *Calculation H*, we do not calculate the propagation of CRs from the local source and assume that its flux contains no secondary species. However, this calculation is very different from all other, because the *low-energy* CRs are a mix of particles which have undergone Galactic propagation and recently accelerated particles from the local source. Because of that the propagation parameters for this calculation should be estimated simultaneously with the parameters of the local source, as in Moskalenko et al. (2003).

Indeed, assuming that CRs from the local source are produced so recently that they contain no secondary nuclei, and that there is no primary boron in CRs, one can calculate the B/C ratio for *Scenario L* in the energy range where the local source contribution is non-negligible. Matching the B/C ratio in the D-R is quite challenging because the local source contribution reduces the B/C ratio in the range 1–10 GeV nucleon^{-1}. This reduction may be compensated by assuming a lower diffusion coefficient in this energy range. At the same time, the diffusion coefficient above 10 GeV nucleon^{-1} cannot be changed very much in order to maintain agreement with high-energy B/C data. The above considerations necessitate a larger value of δ_1. With a greater δ_1, the diffusive reacceleration of low-energy protons becomes too strong, resulting in an overprediction of the proton flux around 1 GeV, and thus v_{Alf} should be reduced. In fact, we found that in this scenario, the best agreement with the PAMELA data for protons is achieved with $v_{\mathrm{Alf}} = 0$ (i.e., no reacceleration) and δ_0=0 below a 4 GV (i.e., the PD model). This is because any finite v_{Alf} hardens the proton spectrum below 1 GeV too much to match the PAMELA data.

Considering the above, we chose to keep *Calculation L* in the D-R model with unchanged diffusion coefficient, in order to illustrate the problem in the B/C fitting. And in the PD model, the reduction of the B/C ratio below 1 GeV was beneficial for agreement with data, because in all other PD calculations, B/C was overpredicted. Quantitatively matching the *ACE* data in the PD model requires the flux of the local source to be relatively small. This dictates our choice of a concave Galactic source spectrum for the *Calculation L* in the PD model, i.e., $g_0 < g_1$ (see Table 2). Such a spectrum is similar to the theoretical predictions by Ptuskin et al. (2010).

Finally, in *Calculation* S_1 (discussed in Section 2.2) all parameters are the same as in *Calculation R*, except for the diffusion coefficient D_0 and the Alfvén speed v_{Alf}. D_0 is reduced by approximately 25%, which makes the ratio z_H/D_0 equal to that in the calculations of Blasi & Amato (2012a). v_{Alf} is reduced accordingly to avoid a large bump in the proton spectrum at low energies. In addition, the propagation calculations use a different set of total inelastic cross sections (Equations [6]–[8] in Hörandel et al. 2007). *Calculation* S_2 has the same parameters as *Calculation* S_1, but the density of all gas components in the Galactic disk (i.e., H I, H II, and H_2) is multiplied by 2. The results of *Calculation* $S_{1,2}$ are compared with *Calculation R* in Figure 7.

4. RESULTS

The results of *Calculations R, S, P, I, L,* and *H,* as specified in Tables 1 and 2, are summarized in Figures 4 through 14. Figures 4 and 5 show the proton and He spectra and their ratio, and Figure 6 shows the CR electron spectrum. Figure 7, illustrating *Hypothesis S*, is discussed in detail in Section 2.2 and in the figure caption.

Since the origin of the difference between the slopes of the proton and He spectra was discussed in detail in Section 2.2, we do not mention that topic in this section, instead concentrating on scenarios explaining the spectral break. *Calculations P, I, L* and *H* were designed to reproduce the observed proton, He and electron spectra and, therefore, cannot be used to constrain any of these scenarios. However, their predictions for CR anisotropy and the production of secondary species (B/C ratio, $\bar{p}$ flux, $\bar{p}/p$ ratio, e^+ flux and $e^+/(e^+ + e^-)$ ratio) differ. These predictions are shown in Figures 8–13. Predictions for the diffuse Galactic γ-ray emission at intermediate

latitudes ($10^\circ < |b| < 20^\circ$) are compared with the data collected by the *Fermi*-LAT in Figure 14.

4.1. *Proton and He Spectra*

Proton and He spectra calculated for the different scenarios and their ratio are plotted in Figures 4 and 5. The bins in rigidity for protons are different from the bins for He in all experiments. Because of this, the experimental data points of PAMELA, ATIC-2, and CREAM shown in Figure 5 were obtained by interpolating the proton and He spectra, along with their errors, and by calculating the p/He ratio on a grid. For simplicity, solar modulation for all spectra is taken into account using the force-field approximation (Gleeson & Axford 1968) with a modulation potential $\Phi = 450$ MV.

While the reference case, *Calculation R*, provides satisfactory agreement with pre-PAMELA data by construction, it naturally misses all newly discovered features: an overall harder He spectrum, the spectral break at $\rho_{\rm br}$, along with the dip just below $\rho_{\rm br}$. The difference between the spectrum of He and protons at all energies was phenomenologically included in all other calculations except *Calculation R*, which is reflected in the considerably better agreement with the p/He ratio data in Figure 5.

Calculation P. A break in the rigidity dependence of the diffusion coefficient leads to a corresponding break in the CR spectrum at Earth. In order to match the data, we assumed the change in the value of δ (see Equation (5)) from $\delta_1 = 0.30$ to $\delta_2 = 0.15$ at $\rho_1 \approx \rho_{\rm br}$. For the PD model, the index changed at ρ_1 from $\delta_1 = 0.60$ to $\delta_2 = 0.37$. The difference $\delta_1 - \delta_2$ is greater in the PD than in the D-R model, because in the latter the reacceleration process additionally softens the spectrum of protons below ρ_0. Two corresponding physical quantities can be derived from these values. Assuming that the change in δ is caused by a difference between the properties of interstellar MHD turbulence on scales smaller and larger than a certain length scale $\Lambda_{\rm br}$, we can estimate this length to be of order of the gyroradius of 300 GV particles. The gyroradius of a particle of rigidity ρ in magnetic field B is

$$r_g = 4 \times 10^{-2} \left(\frac{\rho}{1\,\mathrm{GV}}\right) \left(\frac{B}{5\,\mu\mathrm{G}}\right)^{-1} \mathrm{AU}. \qquad (6)$$

For a characteristic interstellar magnetic field of order of a few μG, this implies a change in turbulence properties on length scales of the order of $\Lambda_{\rm br} \approx 10$ AU. If the quasilinear theory of turbulent particle diffusion applies to CR transport in the ISM, the value $\delta_2 = 0.15$ corresponds to turbulence spectral index, $\alpha = -2 + \delta_2 = -1.85$, which is harder than a Kolmogorov spectrum, $\alpha = -5/3$. Note that the direction in which the index α changes across the transition wavenumber $k = \Lambda_{\rm br}^{-1}$ is opposite to the transition of the turbulent cascade from the inertial to dissipative regime. In our case, the turbulence spectrum must harden, rather than soften, above $k = \Lambda_{\rm br}^{-1}$.

Calculation I assumes a change of the power-law index of CR injection spectrum at $\rho_{\rm inj1} = 300$ GV, which produces a break at $\rho_{\rm br} \approx \rho_{\rm inj1}$ in the CR spectrum at Earth. The dip is not produced in this calculation.

Calculation L (dashed orange lines in Figures 4 and 5) agrees with the p/He ratio and spectral break, and also reproduces the dip just below $\rho_{\rm br}$. This is possible because of the combination of the hard spectrum from Galactic sources that matches the data for $\rho > \rho_{\rm br}$ (solid orange lines in Figure 4) with a local low-energy source having a sharp turnover just below $\rho_{\rm br}$ (dotted orange lines in Figure 4).

In *Calculation H*, the spectral break at $\rho_{\rm br}$ is produced by the local source beginning to dominate the CR spectrum above $\rho_{\rm br}$. We assume that the Galactic source has the same power-law index for $\rho > \rho_{\rm br}$ as the low-energy CR spectrum.

The observed continuity of the p/He ratio and its slope at $\rho_{\rm br}$ within statistical and systematic uncertainties is very important. In *Scenario P*, this property of the p/He ratio comes about naturally. Indeed, if the injection spectrum is continuous, then protons and He nuclei experience the change in diffusion coefficient in the same way, and the p/He ratio is unaffected. However, matching this observation in the framework of a composite source spectrum (*Scenario L*, *Scenario H*, or *Scenario I* (b)) requires an additional assumption of the H to He ratio to be the same at the sources producing the low-energy and high-energy particles.

For the analysis of all calculations discussed above, the dip in the spectrum, if it is significant, may lead to important implications. One possible explanation for the dip may be provided in the framework of *Scenario L* and *Scenario I* (b). It can naturally appear if the spectrum of the low-energy CR sources (local, as in *Scenario L*, or Galactic, as in *Scenario I* (b)) sharply turns over just below $\rho_{\rm br}$, rather than continuing as a power law up to the knee in the CR spectrum. Indeed, it is trivial to prove that for any two power-law spectra, their sum always hardens with energy. Thus, for the softening below $\rho_{\rm br}$ to occur, the low-energy source spectrum may not be a pure power law; the sharpness of the dip suggests that it must steeply turn over below $\rho_{\rm br}$, where the dip occurs. The dip may also be explained in the framework of *Scenario P*, if a corresponding dip in the spectrum of MHD turbulence responsible for CR confinement in the Galaxy is assumed. It is not possible to explain the dip with *Scenario H* because the low-energy source is assumed to have a power-law spectral shape extending all the way to the knee.

4.2. *Electrons*

The CR electron spectrum in this problem is connected to the proton spectrum because (1) electrons propagate in the Galaxy in the same magnetic fields as nuclei, and (2) some, if not all, CR electrons are produced by the same sources as nuclei.

As Figure 6 shows, the propagated electron spectrum in *Calculation R* does not fit the observations of the *Fermi*-LAT (Ackermann et al. 2010) or PAMELA (Adriani 2011). Indeed, the observed spectrum appears convex (i.e., hardening with increasing particle energy) from $\approx$10 to 10^3 GeV, whereas the calculated spectrum in this energy range is concave. The concavity is caused by energy losses on ionization at low energies, and synchrotron losses at high energies.

In *Calculation P*, despite a break in the diffusion coefficient, the electron spectrum at Earth does not fit the high-energy data and is not convex (Figure 6). This is because synchrotron energy losses above 100 GeV oppose the effect of the diffusion coefficient break, and cause the spectral softening.

In the injection effects Scenario, represented by *Calculation I*, it is possible to modify the source spectrum of electrons in order to fit the data. Indeed, since the nucleon injection spectrum has a break at $\rho_{\rm br}$, it is natural to assume that the electron injection spectrum may have a similar feature. This argument holds both in the source with a spectral break interpretation (*Scenario I* (a)) and the composite spectrum in-

terpretation (*Scenario I* (b)) of *Calculation I*. Moreover, the energy and magnitude of the break do not have to be the same for electrons and protons because the electron to proton ratio may vary with energy and with source type. As Figure 6 shows, one can achieve agreement with the data by assuming that the electron source spectrum has a break (hardening) at $R = 70$ GV (61 GV in the PD model), with the index changing from -2.70 to -2.33 (or -2.67 to -2.24 for PD). Note that one cannot justify such a break in any other scenario, unless CR electrons and nuclei are assumed to be produced by different sources.

In *Calculation L*, we assumed that above the break ($\gtrsim$ 100 GV for electrons) the particles are produced by a hard Galactic source, and that below the break the electron flux is dominated by an unknown *low*-energy local source. Likewise, in *Calculation H*, an unknown *high*-energy source of CR electrons was assumed. In both cases, the flux of the local source was calculated as the difference between the observed and the calculated Galactic source fluxes. Therefore, the total spectrum agrees with the data at all energies. Note that only the Galactic source flux was used in the calculation of secondary lepton production and γ-ray emission.

4.3. *Anisotropy*

For all scenarios, we calculated the anisotropy of the high-energy CR flux at the location of the Sun due to diffusive escape of CRs from the Galaxy. The results are presented in Figure 8, along with data. References to individual experiments may be found in Ptuskin et al. (2006a); see also Strong et al. (2007) for a color version of the plot. The anisotropy, dominated by the radial component, is highly sensitive to the choice of the diffusion coefficient and the spatial distribution of CR sources.

Our calculation ignores the effect of nearby CR sources, which may be significant (Ptuskin et al. 2006a; Blasi & Amato 2012b), but is not very well defined and depends on the assumed distances to the sources and their ages. However, if the diffusive component of the anisotropy dominates in a certain energy range, two conclusions may be drawn from this plot. The first one is that *Scenario P* can be distinguished from the others with improved CR proton anisotropy data. The second point illustrated by our calculation is that the diffusion regime of *Calculation P* with $D \propto \rho^{\delta_2}$ and $\delta_2 = 0.15$ agrees with the available data better than $\delta_2 = 0.30$. The PD model, due to a harder dependence of the diffusion coefficient on rigidity, predicts a higher degree of anisotropy, which disagrees with the data more than the other calculations.

In the case of *Calculation H*, the plotted lines correspond to only the Galactic source, while the direction and magnitude of the local source flux anisotropy above $\rho_{\rm br}$ are unknown. Depending on the location and proximity of the local source, the direction of the overall CR drift can be changed substantially, because the local source flux above 10^3 GV is comparable to the Galactic flux (see the bottom plots in Figure 4). Since the estimate of the distance to the local source is beyond the scope of this paper, we do not provide quantitative predictions of anisotropy in this case.

4.4. *Boron to Carbon Ratio*

The B/C ratio for all scenarios discussed in the paper is shown in Figure 9. Predictions of *Calculation R* and *Calculation I* coincide at all energies, while *Calculation P* predicts a larger B/C ratio for $\rho > \rho_{\rm br}$, which is a consequence of the smaller diffusion coefficient in *Calculation P*. In the case of *Calculation L* and *Calculation H*, the results include the effect of the local CR source. CR boron is produced by fragmentation of heavier elements and decay of ^{10}Be. If the local source is very nearby, its flux should contain no boron. However, the abundance of (primary) carbon should be close to the interstellar value, which results in a lower B/C ratio in the net flux than without the local source.

To find the B/C ratio for *Calculation H* and *Calculation L*, we assume that the local source produces no boron and assume that the flux of local source carbon is proportional to that of He, with the same carbon and He abundance as in the Galactic source. *Calculation H* predicts a lower B/C for $\rho > \rho_{\rm br}$ because the local high-energy source supplies primary carbon, but not secondary boron, at these energies. *Calculation L* could not be tuned to reproduce the B/C ratio in the D-R model (see Section 3.3) However, in the PD model, the only calculation fitting the B/C ratio below 1 GeV nucleon^{-1} is *Calculation L* due to the reduction of the B/C ratio by the local source.

Experimental data at low energies (below 1 GeV nucleon^{-1}) were collected by *ACE* (Davis et al. 2000), and for high energies by *HEAO-3* (Engelmann et al. 1990), CREAM (Ahn et al. 2008), ATIC-2 (Panov et al. 2008), and TRACER (Obermeier et al. 2011). The uncertainties in the data are still too large to rule out any of the scenarios considered in this paper, but data collected by future experiments, such as AMS-2, may be more constraining.

4.5. *Antiproton Flux and $\bar{p}/p$ Ratio*

The antiproton flux, another probe of CR propagation, is plotted in Figure 10, and $\bar{p}/p$ ratio in Figure 11, together with the PAMELA data from Adriani et al. (2010) and the BESS-Polar II data from Abe et al. (2011). *Calculations R, P, I,* and *H* are in good agreement with data below 100 GeV. Differences between all calculations are apparent above $\sim$1 TeV, but no data are currently available.

Calculation L, the only case of the PD model where the low-energy B/C data are reproduced, predicts a factor of ~ 2 excess of $\bar{p}$ below 100 GeV, due to a larger particle confinement time. In *Calculations L* and *H*, the local source was assumed to be completely devoid of primary or secondary antiprotons. More accurate data covering a larger energy range may help eliminate some of the scenarios, and the AMS-2 mission may provide these data.

4.6. *Positrons*

Figure 12 shows the calculated positron flux, and Figure 13 — the positron fraction ($e^+/(e^- + e^+)$). Our model does not include a source of primary CR positrons; the e^+ particles in all our calculations are produced in inelastic collisions of other CR species.

The positron flux measured by the *Fermi*-LAT (Ackermann et al. 2012) is significantly greater than the prediction of all our calculations (Figure 12). The only scenario that could explain the discrepancy is *Scenario H* in which the local high-energy CR source produces *primary* positrons.

The positron fraction (Figure 13) provides additional evidence that the calculations predict insufficient flux of positrons at high energies. However, below a few GeV, the positron fraction in the D-R model is overpredicted.

4.7. *Diffuse γ-Ray Emission*

Predictions of the γ-ray emission at intermediate Galactic latitudes ($10^\circ < |b| < 20^\circ$) are plotted in Figure 14 along with the data reported by Abdo et al. (2010, see the online supplementary material). Following Abdo et al. (2010), the flux of the inverse Compton (IC) component was increased by a factor of two to obtain a good fit to the data. Our calculations include γ-ray emission produced by hadronic and leptonic components of CRs (i.e., π^0-decay, IC, and bremsstrahlung channels), as well as point sources, and the isotropic extragalactic emission. The relative differences in the *total* γ-ray flux between the considered scenarios are quite small and are considerably smaller than if only the π^0-decay channel is considered (as in Donato & Serpico 2011).

Predictions of all calculations, except *Calculation L*, agree with the published *Fermi*-LAT data, within the uncertainty band. *Calculation L* predicts a slightly lower γ-ray emission below 10 GeV. Note that even the reference *Calculation R*, which does not agree with the PAMELA data, satisfactorily reproduces the γ-ray data.

For all scenarios we calculated the γ-ray spectrum up to 1 TeV, but the *Fermi*-LAT team has not published on the data above 100 GeV so far. At these energies, the softer spectrum of protons (above $\rho_{\rm br}$) from Galactic sources in *Calculation H* produces less pions resulting in a smaller flux of pionic γ-rays compared to other scenarios. However, the contributions of comparable IC component and isotropic emission in the range 100 GeV – 1 TeV are not affected by the proton spectrum. Therefore, even at these energies the difference between the *total* γ-ray emission in *Calculation H* and other calculations is significantly smaller than the difference in the π^0-decay channel alone. Unsurprisingly, *Calculation P* cannot be distinguished from *Calculation I* using the γ-ray data alone, because calculations for both scenarios result in nearly the same spectrum of CR protons, even though it is achieved via different mechanisms.

As the *Fermi* mission continues, the statistical uncertainty will be reduced as data accumulates, and systematic errors are likely to be brought down by improved data analysis. It should be noted, however, that the analysis of the diffuse γ-ray emission is complicated by many factors, including the uncertainty in the spatial distribution for the CR sources and the loosely constrained spectrum of CR electrons over the Galaxy responsible for IC emission that dominates high-energy γ-rays.

5. SUMMARY

We have presented scenarios reproducing the spectral features in CR proton and He spectra (the p/He ratio dependence on energy, the dip, and spectral break) observed by ATIC-2, CREAM, and PAMELA. For each scenario, we performed CR propagation calculations in the framework of the D-R model (except *Scenario L*), using the GALPROP code. Differences between scenarios are reflected in the CR anisotropy and fluxes of secondary CR species: the B/C ratio at high energies, the antiproton flux and antiproton to proton ratio, as well as the diffuse Galactic γ-ray emission. We find the following:

(1) He spallation (*Hypothesis S*) may be partially responsible for making the spectrum of He and heavier nuclei harder than protons. However, a significantly increased grammage traversed by CRs in the Galaxy is required to explain the p/He observations with spallation alone. This makes it problematic to match stable secondary CR isotope observations (B/C and antiprotons).

(2) Electron spectrum can be reproduced in *Scenario I* (a) (break in the injection spectrum) or *Scenario I* (b) (composite Galactic source) only if the break in the electron injection spectrum is stronger, and occurs at a lower rigidity, than in the proton spectrum. A break in the diffusion coefficient (*Scenario P*) cannot simultaneously explain the concavity of the observed proton and electron spectra.

(3) Experimental uncertainty in the data on high-energy B/C ratio does not allow us to rigorously reject any of the scenarios for the origin of the spectral break. However, more accurate measurements of high-energy B/C, expected from planned CR experiments, may be used for model rejection.

(4) In the D-R model, low-energy B/C data are consistent with any scenario except *Scenario L* (low-energy local source). In the PD model, low-energy B/C data require that the diffusion coefficient decreases with increasing energy; however, it is also possible to achieve agreement with these data in *Scenario L* for constant diffusion coefficient.

(5) Antiproton flux and $\bar{p}/p$ ratio seem to disfavor the low-energy local source hypothesis (*Scenario L*). Measurements of $\bar{p}$ and/or $\bar{p}/p$ above 1 TeV may help to differentiate between the other scenarios.

(6) Radial component of the diffusive anisotropy of CR flux is too high in all scenarios, but the discrepancy is larger in *Scenario L*, while *Scenario P* predicts the lowest anisotropy. The PD model predicts a higher anisotropy than the D-R model. Local sources may significantly affect the CR anisotropy, and therefore our simple analysis applies only to energy range unaffected by local sources.

(7) Data on the positron flux and positron fraction are inconsistent with any of the scenarios, if all observed CR positrons are secondary. However, if some of the detected positrons are produced in sources, then only *Scenario H* (local high-energy source) can account for the observed positron excess at high energies.

(8) Finally, the γ-ray data are in agreement, within the uncertainty range, with all scenarios, including *Scenario R*, even though the reference scenario does not agree with the new measurements for the CR proton and He spectra. *Scenario L* slightly underpredicts the γ-ray flux below a few GeV.

Most specific physical models explaining the p/He ratio, spectral break and the dip fall into one of the scenarios studied in this paper, or their combination. Data from experiments such as the *Fermi*-LAT and AMS-2 can be used to distinguish between some of these scenarios.

A. V. and I. V. M. acknowledge support from NASA grant no. NNX09AC15G. T. A. P. acknowledges support from NASA grant no. NNX10AE78G. The authors are grateful to P. Blasi, E. Orlando, and A. Strong for fruitful discussions and to P. Picozza and M. Boezio for sharing and discussing preliminary PAMELA results. The authors thank the anonymous referee for constructive comments.

REFERENCES

Abbasi, R., et al. 2005, Physics Letters B, 619, 271
Abbasi, R. U., et al. 2009, Astroparticle Physics, 32, 53
Abdo, A. A., et al. 2009, Physical Review Letters, 103, 251101
—. 2010, Physical Review Letters, 104, 101101
Abe, K., et al. 2011, ArXiv: 1107.6000
Abraham, J., et al. 2010, Physics Letters B, 685, 239
Ackermann, M., et al. 2010, Phys. Rev. D, 82, 092004
—. 2012, Physical Review Letters, 108, 011103

Adriani, O., et al. 2009, Nature, 458, 607
—. 2010, Physical Review Letters, 105, 121101
—. 2011, Science, 332, 69
Adriani, O. o. 2011, Physical Review Letters, 106, 201101
Ahn, H. S., et al. 2008, Astroparticle Physics, 30, 133
—. 2009, ApJ, 707, 593
—. 2010, ApJ, 714, L89
Alcaraz, J., et al. 2000, Physics Letters B, 490, 27
Barashenkov, V. S. 1993, Cross Sections of Interactions of Particles and Nuclei with Nuclei, JINR, Dubna, Russia, p. 346, in Russian
Barashenkov, V. S., & Polyanski, A. 1994, CROSEC code, Joint Institute for Nuclear Research, JINR E2-94-417
Berezinskii, V. S., Bulanov, S. V., Dogiel, V. A., & Ptuskin, V. S. 1990, Astrophysics of cosmic rays (Amsterdam: North-Holland, 1990, edited by Ginzburg, V. L.)
Biermann, P. L., Becker, J. K., Dreyer, J., Meli, A., Seo, E.-S., & Stanev, T. 2010, ApJ, 725, 184
Biermann, P. L., Gaisser, T. K., & Stanev, T. 1995, Phys. Rev. D, 51, 3450
Biskamp, D. 2003, Magnetohydrodynamic Turbulence (Cambridge University Press)
Blasi, P., & Amato, E. 2012a, JCAP, 1, 10
—. 2012b, JCAP, 1, 11
Caprioli, D., Amato, E., & Blasi, P. 2010, Astroparticle Physics, 33, 160
Case, G. L., & Bhattacharya, D. 1998, ApJ, 504, 761
Davis, A. J., et al. 2000, in American Institute of Physics Conference Series, Vol. 528, Acceleration and Transport of Energetic Particles Observed in the Heliosphere, ed. R. A. Mewaldt, J. R. Jokipii, M. A. Lee, E. Möbius, & T. H. Zurbuchen , 421–424
Donato, F., & Serpico, P. D. 2011, Phys. Rev. D, 83, 023014
Drury, L. O., et al. 2001, Space Sci. Rev., 99, 329
Ellison, D. C., Drury, L. O., & Meyer, J. 1997, ApJ, 487, 197
Elmegreen, B. G., & Scalo, J. 2004, ARA&A, 42, 211
Engelmann, J. J., Ferrando, P., Soutoul, A., Goret, P., & Juliusson, E. 1990, A&A, 233, 96
Gleeson, L. J., & Axford, W. I. 1968, ApJ, 154, 1011
Haino, S., et al. 2004, Physics Letters B, 594, 35
Haungs, A., Rebel, H., & Roth, M. 2003, Reports on Progress in Physics, 66, 1145
Hörandel, J. R., Kalmykov, N. N., & Timokhin, A. V. 2007, Astroparticle Physics, 27, 119
Iroshnikov, P. S. 1964, Soviet Ast., 7, 566
Kolmogorov, A. 1941, Akademiia Nauk SSSR Doklady, 30, 301
Kraichnan, R. H. 1965, Physics of Fluids, 8, 1385
Kulikov, G. V., & Khristiansen, G. B. 1958, Soviet Physics JETP, 35, 635
Malkov, M. A., Diamond, P. H., & Sagdeev, R. Z. 2012, Physical Review Letters, 108, 081104
Moskalenko, I. V., Strong, A. W., Mashnik, S. G., & Ormes, J. F. 2003, ApJ, 586, 1050
Moskalenko, I. V., Strong, A. W., Ormes, J. F., & Potgieter, M. S. 2002, ApJ, 565, 280
Obermeier, A., et al. 2011, ApJ, 742, 14
Ohira, Y., & Ioka, K. 2011, ApJ, 729, L13+
Panov, A. D., et al. 2008, in International Cosmic Ray Conference, Vol. 2, 3–6
Panov, A. D., et al. 2009, Bulletin of the Russian Academy of Science, Phys., 73, 564
Press, W. H., Teukolsky, S. A., Vetterling, W. T., & Flannery, B. P. 1992, Numerical recipes in FORTRAN. The art of scientific computing (Cambridge: University Press, —c1992, 2nd ed.)
Ptuskin, V., Zirakashvili, V., & Seo, E. 2010, ApJ, 718, 31
Ptuskin, V. S., Jones, F. C., Seo, E. S., & Sina, R. 2006a, Advances in Space Research, 37, 1909
Ptuskin, V. S., Moskalenko, I. V., Jones, F. C., Strong, A. W., & Zirakashvili, V. N. 2006b, ApJ, 642, 902
—. 2006c, ApJ, 642, 902
Ptuskin, V. S., & Soutoul, A. 1998, A&A, 337, 859
Scalo, J., & Elmegreen, B. G. 2004, ARA&A, 42, 275
Seo, E. S., & Ptuskin, V. S. 1994, ApJ, 431, 705
Strong, A. W., & Moskalenko, I. V. 1998, ApJ, 509, 212
Strong, A. W., Moskalenko, I. V., & Ptuskin, V. S. 2007, Annual Review of Nuclear and Particle Science, 57, 285
Strong, A. W., Moskalenko, I. V., & Reimer, O. 2004, ApJ, 613, 962
Swordy, S. P. 2001, Space Sci. Rev., 99, 85
Trotta, R., Jóhannesson, G., Moskalenko, I. V., Porter, T. A., Ruiz de Austri, R., & Strong, A. W. 2011, ApJ, 729, 106
Vladimirov, A. E., Digel, S. W., Jóhannesson, G., Michelson, P. F., Moskalenko, I. V., Nolan, P. L., Orlando, E., Porter, T. A., & Strong, A. W. 2011, Computer Physics Communications, 182, 1156
Webber, W. R., & Soutoul, A. 1998, ApJ, 506, 335
Wefel, J. P., Adams, Jr., J. H., Ahn, H. S., & et al. 2008, in International Cosmic Ray Conference, Vol. 2, International Cosmic Ray Conference, 31–34
Wiedenbeck, M. E., et al. 2001, Space Sci. Rev., 99, 15
Yoon, Y. S., et al. 2011, The Astrophysical Journal, 728, 122
Yuan, Q., Zhang, B., & Bi, X.-J. 2011, Phys. Rev. D, 84, 043002

Table 1
Summary of Model Parameters, Diffusive-reacceleration (D-R) Model

Parameter	Description	*Calculations*					
		R	*S_1 (S_2)*	*P*	*I*	*L*	*H*
NUCLEON INJECTION							
g_0 (protons)	Injection index for $\rho < \rho_{\rm inj0}$	–1.90	–1.90	–1.90	–1.90	–1.90	–1.90
$\rho_{\rm inj0}$	First break in CR injection spectrum, GV	11	11	11	11	11	11
g_1 (protons)	Injection index for $\rho_{\rm inj0} < \rho < \rho_{\rm inj1}$	–2.40	–2.40	–2.50	–2.50	–2.35	–2.50
$\rho_{\rm inj1}$	Second break in CR injection spectrum, GV	···	···	···	300	···	···
g_2 (protons)	Injection index for $\rho_{\rm inj1} < \rho$	···	···	···	–2.35	···	···
$\Delta_{p/\rm He}$	For nuclei, $g_i(A>1)$=g_i(protons)+$\Delta_{p/\rm He}$	···	···	0.07	0.07	0.07	0.07
N_p	Flux of protons at $\rho = 10^3$ GV, in units 10^{-12} cm^{-2} sr^{-1} s^{-1} MeV^{-1}	10.7	10.7	8.56	8.56	8.56	7.26
$n({\rm H})/n_0({\rm H})$	Multiplication factor for the gas number density relative to standard gas maps	···	$^{1.0}_{(2.0)}$	···	···	···	···
^{4}He/^{1}H	Abundance of ^{4}He relative to ^{1}H in CR sources at 10^3 GeV nucleon^{-1}. Abundances of other isotopes are proportional to ^{4}He.	0.0686	$^{0.0910}_{(0.113)}$	0.0842	0.0932	0.0944	0.0830
ELECTRON INJECTION							
$g_{\rm e0}$	Electron injection index for $\rho < \rho_{\rm e0}$	–1.60	–1.60	–1.60	–1.60	···	–1.60
$\rho_{\rm e0}$	Low-energy break for electrons, GV	4	4	4	4	···	4
$g_{\rm e1}$	Injection index for $\rho_{\rm e0} < \rho < \rho_{\rm e1}$	–2.50	–2.50	–2.70	–2.70	···	–2.70
$\rho_{\rm e1}$	Intermediate energy break for electrons, GV	···	···	···	70	···	···
$g_{\rm e2}$	Injection index for $\rho_{\rm e1} < \rho < \rho_{\rm e2}$	···	···	···	–2.33	–2.33	···
$\rho_{\rm e2}$	High-energy break for electrons, GV	2×10^3	2×10^3	2×10^3	2×10^3	2×10^3	2×10^3
$g_{\rm e3}$	Injection index for $\rho_{\rm e2} < \rho$	5.0	5.0	5.0	5.0	5.0	5.0
N_e	Flux of protons at $\rho = R_e$, in units 10^{-9} cm^{-2} sr^{-1} s^{-1} MeV^{-1}	1.100	1.100	1.100	1.166	5.15e-4	1.166
R_e	Rigidity for proton flux normalization, GV	24.8	24.8	24.8	24.8	300	24.8
PROPAGATION							
$v_{\rm Alf}$	Alfvén speed	32	25	32	32	32	32
D_0	Diffusion coefficient in 10^{28} cm^2 s^{-1} at ρ=4 GV	5.75	4.00	5.75	5.75	5.75	5.75
δ_0	δ in Equation (5) for $\rho < \rho_0$	···	···	···	···	···	···
ρ_0	Low energy diffusion coefficient break, GV	···	···	···	···	···	···
δ_1	δ in Equation (5) for $\rho < \rho_0$	0.30	0.30	0.30	0.30	0.30	0.30
ρ_1	High energy diffusion coefficient break, GV	···	···	300.0	···	···	···
δ_2	δ for $\rho > \rho_1$	···	···	0.15	···	···	···

Table 2
Summary of Model Parameters, Plain Diffusion (PD) Model

Parameter	Description	*Calculations*					
		R	S_1 (S_2)	*P*	*I*	*L*	*H*
NUCLEON INJECTION							
g_0 (protons)	Injection index for $\rho < \rho_{\rm inj0}$	···	···	···	···	–2.40	···
$\rho_{\rm inj0}$	First break in CR injection spectrum, GV	···	···	···	···	54	···
g_1 (protons)	Injection index for $\rho_{\rm inj0} < \rho < \rho_{\rm inj1}$	–2.10	–2.10	–2.26	–2.26	–2.05	–2.26
$\rho_{\rm inj1}$	Second break in CR injection spectrum, GV	···	···	···	300	···	···
g_2 (protons)	Injection index for $\rho_{\rm inj1} < \rho$	···	···	···	–2.05	···	···
$\Delta_{p/\rm He}$	For nuclei, $g_i(A>1)$=g_i(protons)+$\Delta_{p/\rm He}$	···	···	0.07	0.07	0.07	0.07
N_p	Flux of protons at $\rho = 10^3$ GV, in units 10^{-12} cm^{-2} sr^{-1} s^{-1} MeV^{-1}	10.7	10.7	8.56	8.56	8.56	6.93
$n({\rm H})/n_0({\rm H})$	Multiplication factor for the gas number density relative to standard gas maps	···	$^{1.0}_{(2.0)}$	···	···	···	···
^{4}He/^{1}H	Abundance of ^{4}He relative to ^{1}H in CR sources at 10^3 GeV nucleon^{-1}. Abundances of other isotopes are proportional to ^{4}He.	0.0888	$^{0.111}_{(0.135)}$	0.103	0.115	0.118	0.0968
ELECTRON INJECTION							
$g_{\rm e0}$	Electron injection index for $\rho < \rho_{\rm e0}$	–1.60	–2.00	–2.00	2.00	···	–2.00
$\rho_{\rm e0}$	Low-energy break for electrons, GV	4	4	4	4	···	4
$g_{\rm e1}$	Injection index for $\rho_{\rm e0} < \rho < \rho_{\rm e1}$	–2.35	–2.35	–2.67	–2.67	···	–2.67
$\rho_{\rm e1}$	Intermediate energy break for electrons, GV	···	···	···	61	···	···
$g_{\rm e2}$	Injection index for $\rho_{\rm e1} < \rho < \rho_{\rm e2}$	···	···	···	–2.24	–2.24	···
$\rho_{\rm e2}$	High-energy break for electrons, GV	2×10^3	2×10^3	2×10^3	2×10^3	2×10^3	2×10^3
$g_{\rm e3}$	Injection index for $\rho_{\rm e2} < \rho$	5.0	5.0	5.0	5.0	5.0	5.0
N_e	Flux of protons at $\rho = R_e$, in units 10^{-9} cm^{-2} sr^{-1} s^{-1} MeV^{-1}	1.100	1.100	1.100	1.166	5.15e-4	1.166
R_e	Rigidity for proton flux normalization, GV	24.8	24.8	24.8	24.8	300	24.8
PROPAGATION							
$v_{\rm Alf}$	Alfvén speed	···	···	···	···	···	···
D_0	Diffusion coefficient in 10^{28} cm^2 s^{-1} at ρ=4 GV	3.00	2.20	3.00	3.00	1.30	3.00
δ_0	δ in Equation (5) for $\rho < \rho_0$	0.0	0.0	0.0	0.0	0.0	0.0
ρ_0	Low energy diffusion coefficient break, GV	4.0	4.0	4.0	4.0	4.0	4.0
δ_1	δ in Equation (5) for $\rho < \rho_0$	0.60	0.60	0.60	0.60	0.60	0.60
ρ_1	High energy diffusion coefficient break, GV	···	···	300.0	···	···	···
δ_2	δ for $\rho > \rho_1$	···	···	0.37	···	···	···

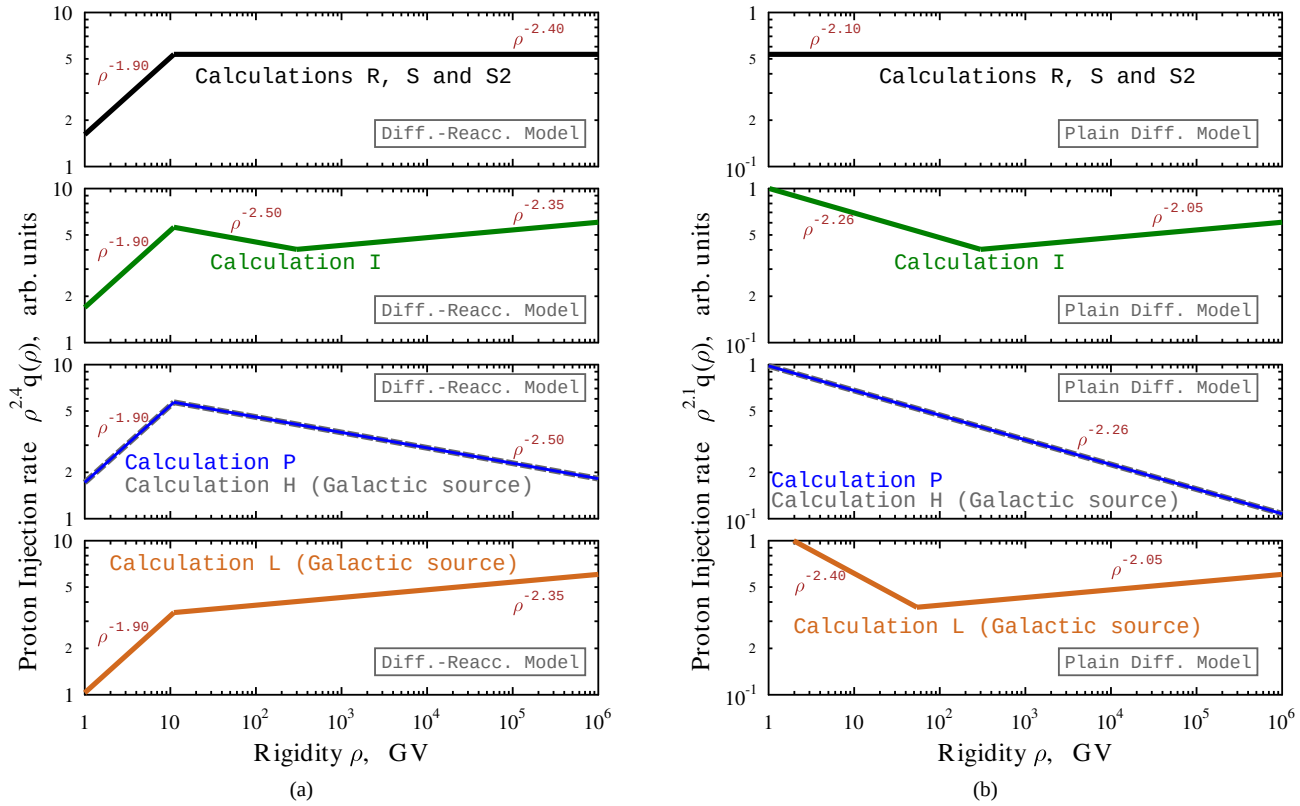

Figure 1. (color in online version) Galactic CR source injection spectrum for *Calculations R, S, P, I, L,* and *H* in arbitrary units. *Left*: diffusive-reacceleration model, *right*: plain diffusion model. The normalization for the injection spectrum was chosen to match local measurements of proton and He spectra. For all calculations, the lines represent the Galactic CR source injection spectrum. "Local" sources, present in *Calculation L* and *Calculation H*, are not shown here. The "local" source fluxes at Earth in *Calculation L* and *Calculation H* were obtained as the difference between the observed and propagated Galactic fluxes.

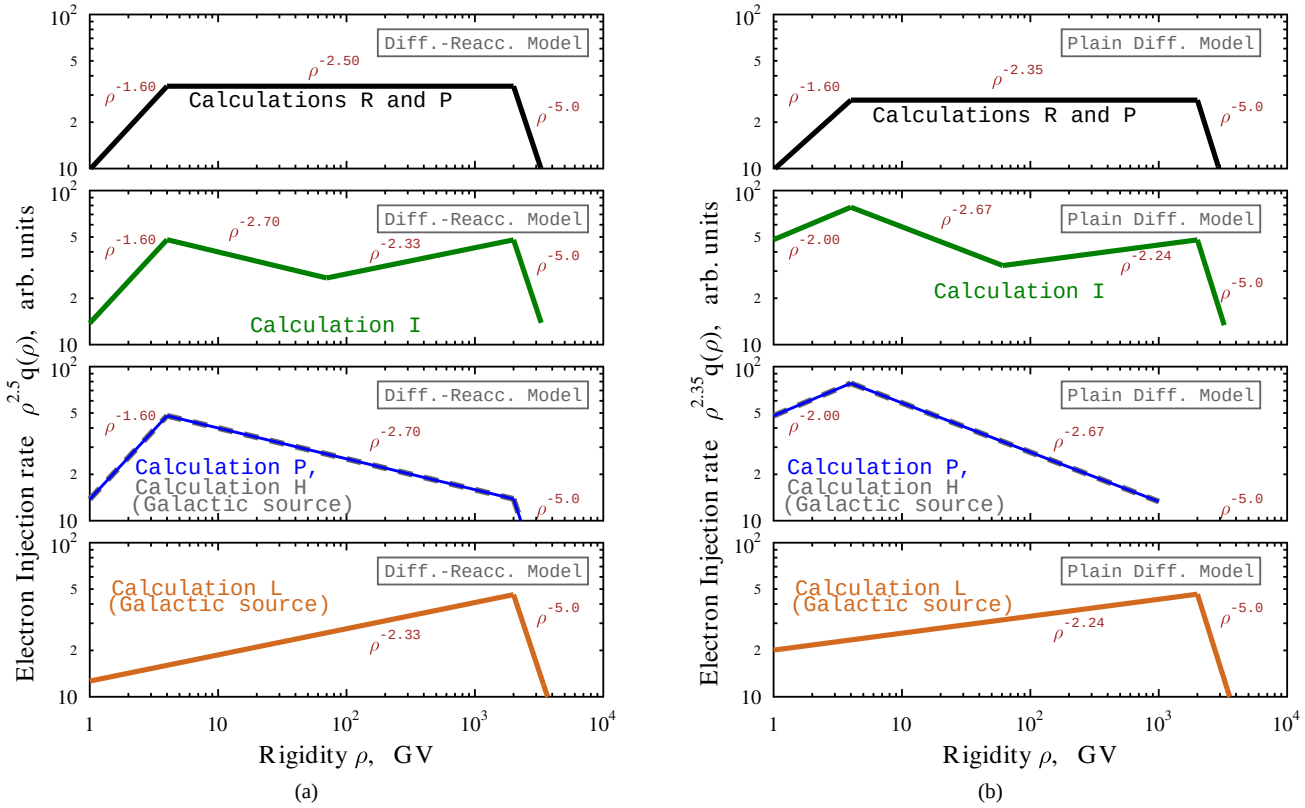

Figure 2. (color in online version) Galactic CR source electron injection spectrum for *Calculations R, S, P, I, L,* and *H* in arbitrary units. *Left*: diffusive-reacceleration model, *right*: plain diffusion model. The normalization for the injection spectrum was chosen to match local measurements of proton and He spectra. For all calculations, the lines represent the Galactic CR source injection spectrum. "Local" sources, present in *Calculation L* and *Calculation H*, are not shown here. The "local" source fluxes at Earth in *Calculation L* and *Calculation H* were obtained as the difference between the observed and propagated Galactic fluxes.

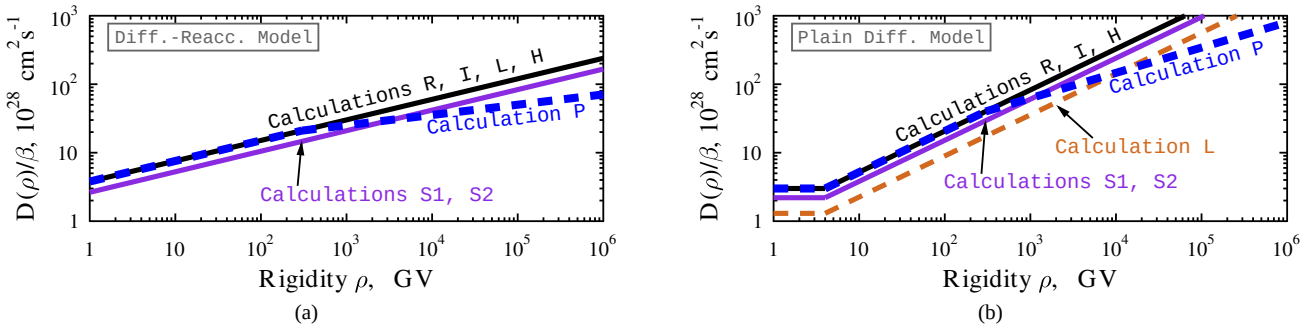

Figure 3. (color in online version) Diffusion coefficient of CRs in the Galaxy (see Equation (5)). *Left*: diffusive-reacceleration model, *right*: plain diffusion model. The values of the D coincide for *Calculations R, I, L* and *H*. For *Calculation S*, the value of D is slightly smaller at all energies. For *Calculation P*, a break in the diffusion coefficient is assumed, changing $\delta_1/\delta_2 = 0.30/0.15$ at $\rho_1 = 300$ GV.

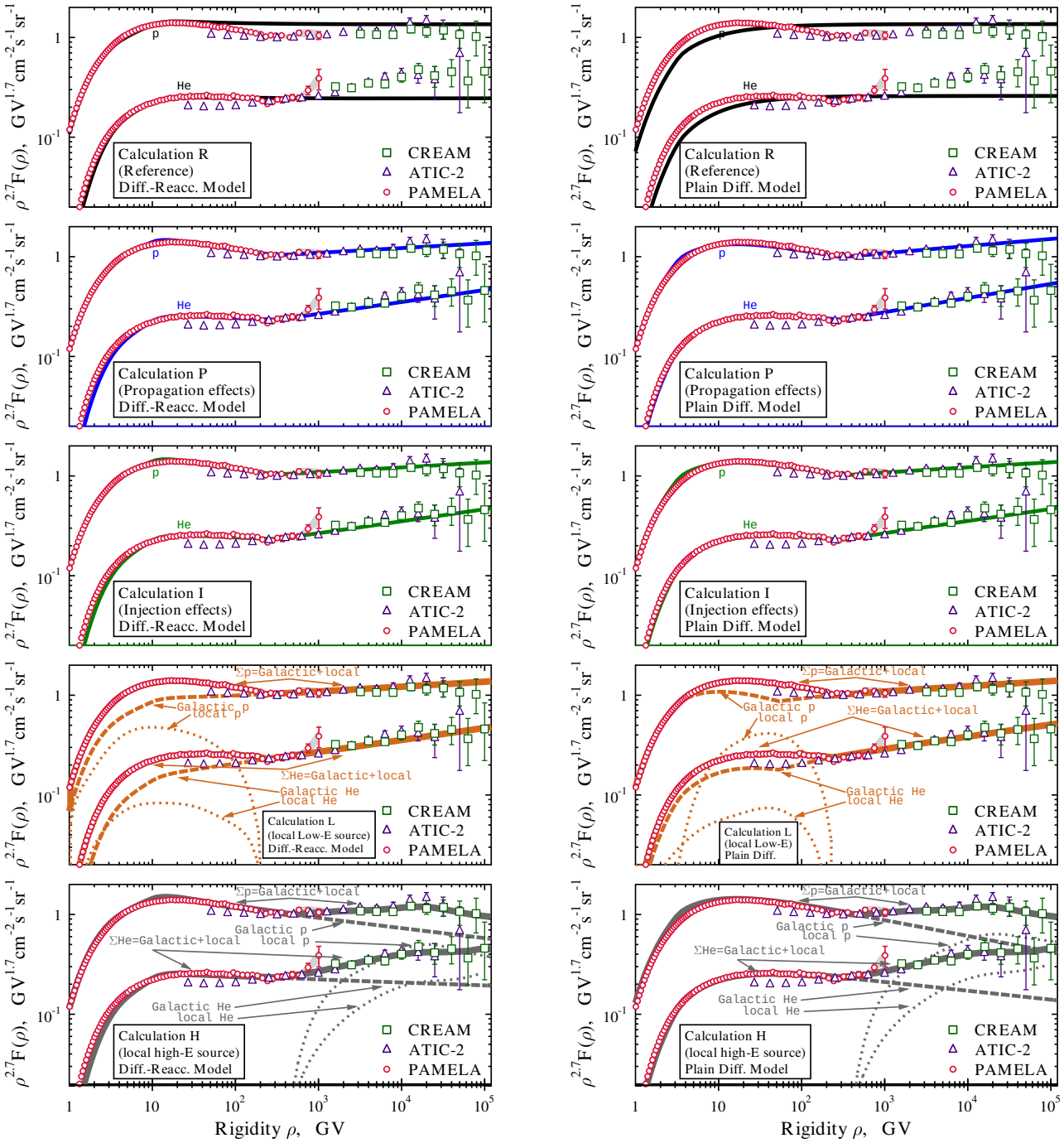

Figure 4. (color in online version) Propagated CR proton and He spectra: data of PAMELA (Adriani et al. 2011), ATIC-2 (Wefel et al. 2008; Panov et al. 2009), and CREAM (Ahn et al. 2010; Yoon et al. 2011) together with calculation results. *Left*: diffusive-reacceleration model, *right*: plain diffusion model. For *Calculations L* and *H*, solid lines show the net CR flux comprised of the Galactic source contribution (dashed lines) and a "local" source contribution (dotted lines). Solar modulation in all spectra is taken into account using force-field approximation with a modulation potential $\Phi = 450$ MV. See the discussion in Section 4.1.

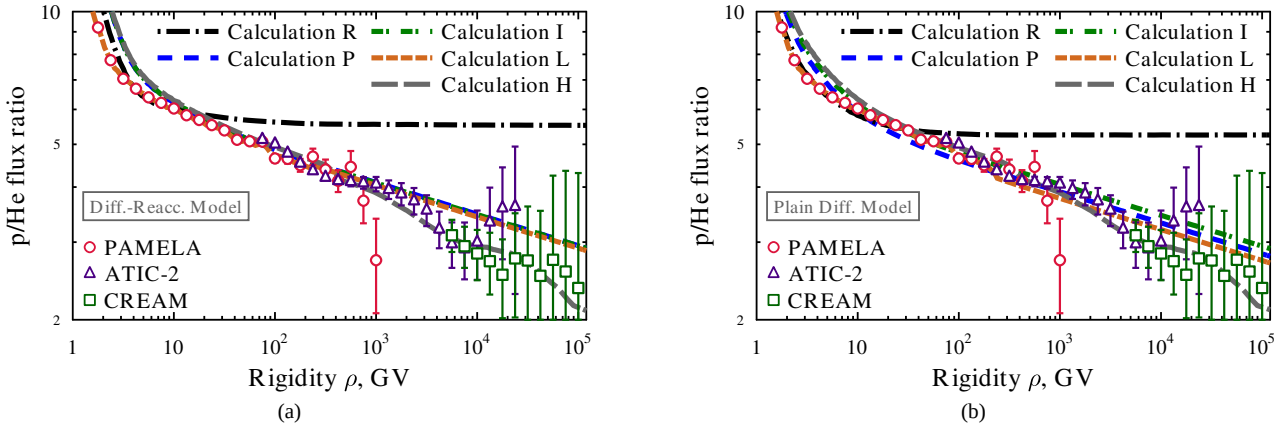

Figure 5. (color in online version) Propagated CR proton to He flux ratio: data of PAMELA (Adriani et al. 2011), ATIC-2 (Wefel et al. 2008; Panov et al. 2009), and CREAM (Ahn et al. 2010; Yoon et al. 2011), together with calculation results. *Left*: diffusive-reacceleration model, *right*: plain diffusion model. The *p*/He points for experimental data were obtained by interpolating the measured fluxes of protons and He along with respective errors and calculating the *p*/He ratio on a grid. See the discussion in Section 4.1.

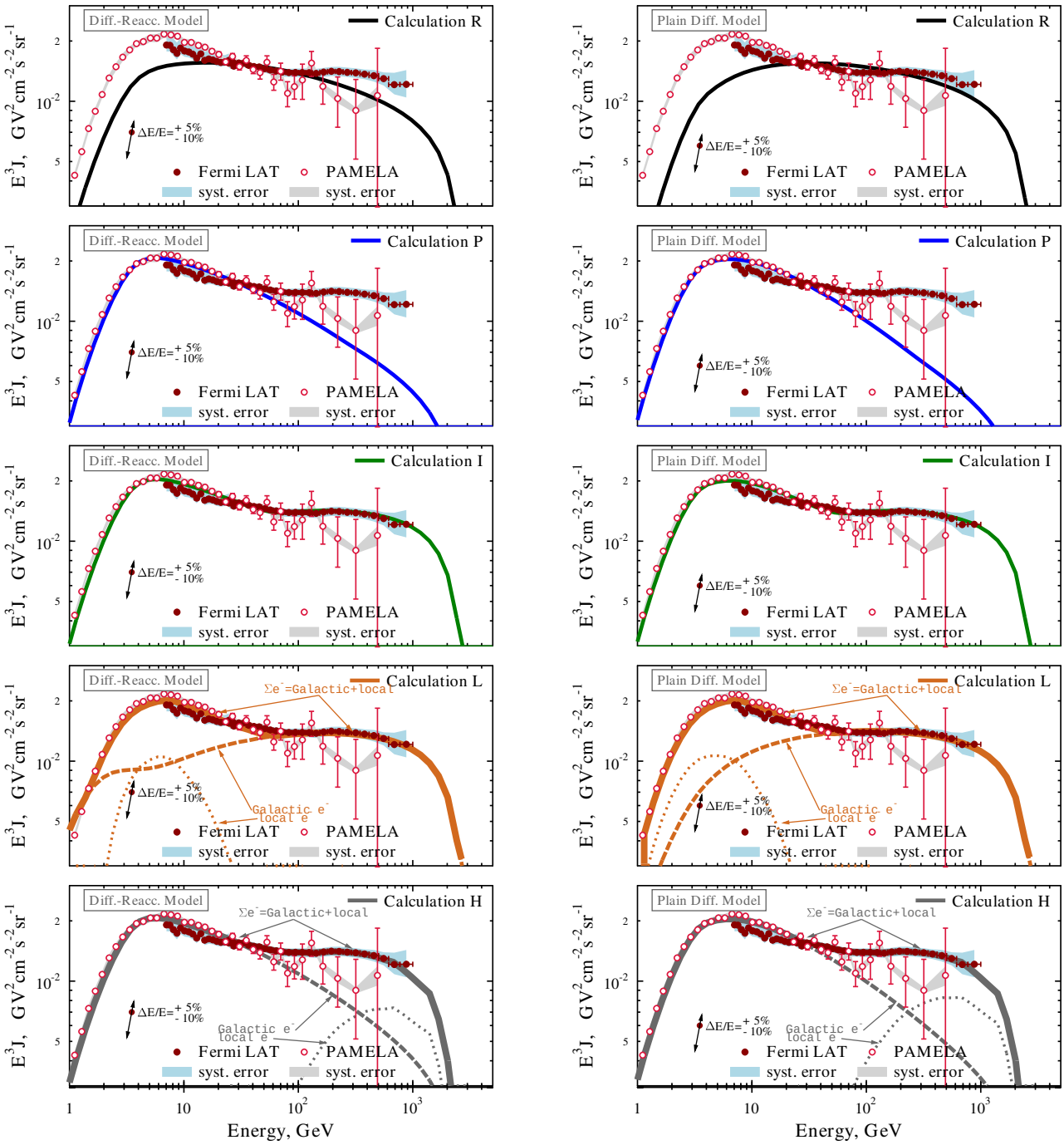

(a) (b)

Figure 6. (color in online version) Propagated CR electron spectra: models and data. *Left*: diffusive-reacceleration model, *right*: plain diffusion model. The data are from Ackermann et al. (2010) (*Fermi*-LAT) and Adriani (2011) (PAMELA). See the discussion in Section 4.2

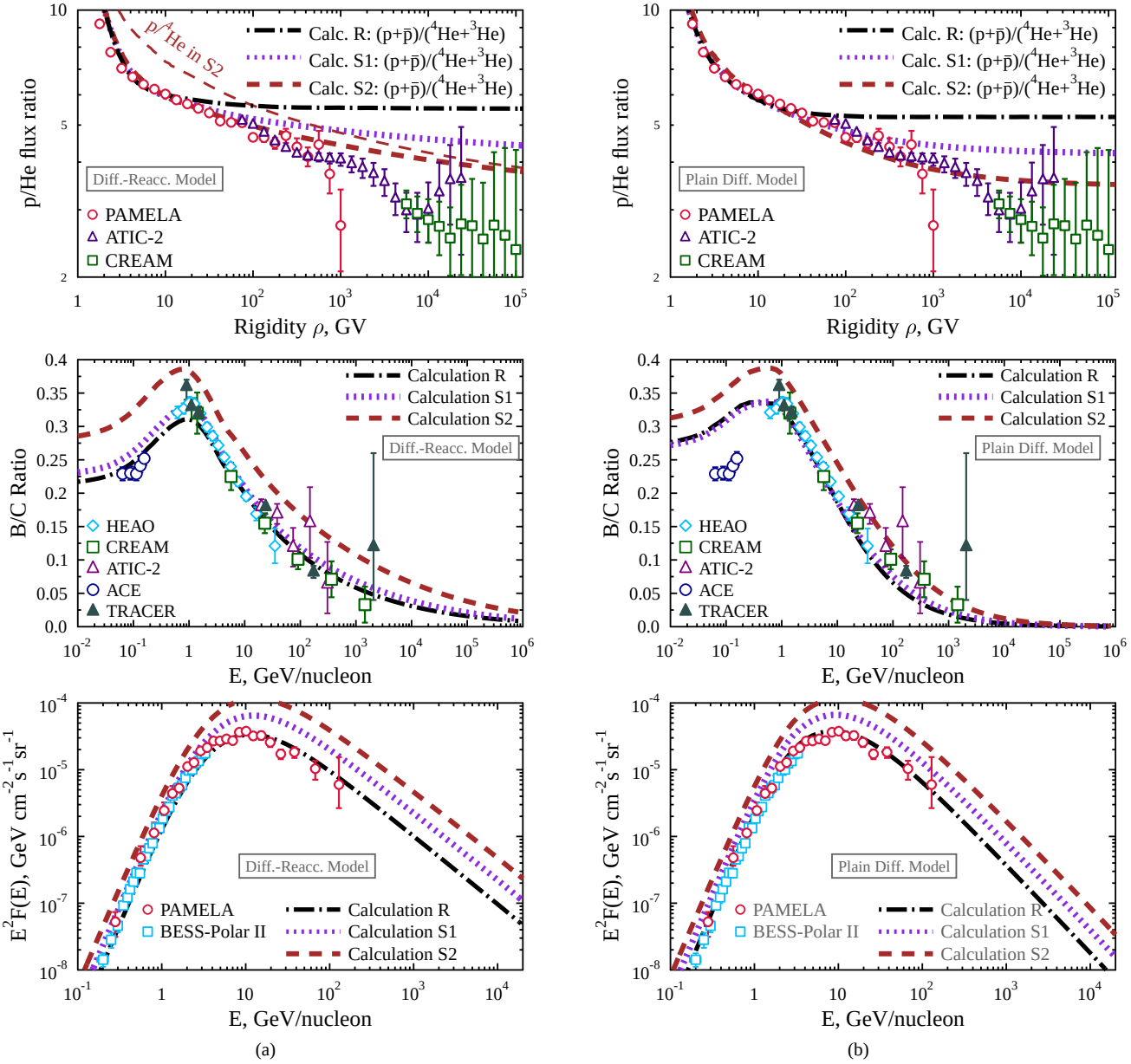

Figure 7. (color in online version) CR proton to He, B/C ratio and antiproton flux (sources of data as in Figures 5, 9, 10), together with calculation results. *Left*: diffusive-reacceleration model, *right*: plain diffusion model. *Calculation* S_1 and *Calculation* S_2 use the same spallation cross sections and $z_H\,/\,D$ ratio as those of Blasi & Amato (2012a). In *Calculation* S_2, the gas density is increased by a factor of 2 with respect to *Calculation* S_1. Results of *Calculation* S_1 are consistent with the B/C ratio data, but slightly overpredict $\bar{p}$ measurements. However, note that the effect of spallation is not sufficient to make the slope of the p/He ratio agree with the PAMELA data. In *Calculation* S_2, spallation is stronger due to increased grammage, and the p/He ratio is reproduced better, but the B/C ratio and $\bar{p}$ flux are overpredicted.

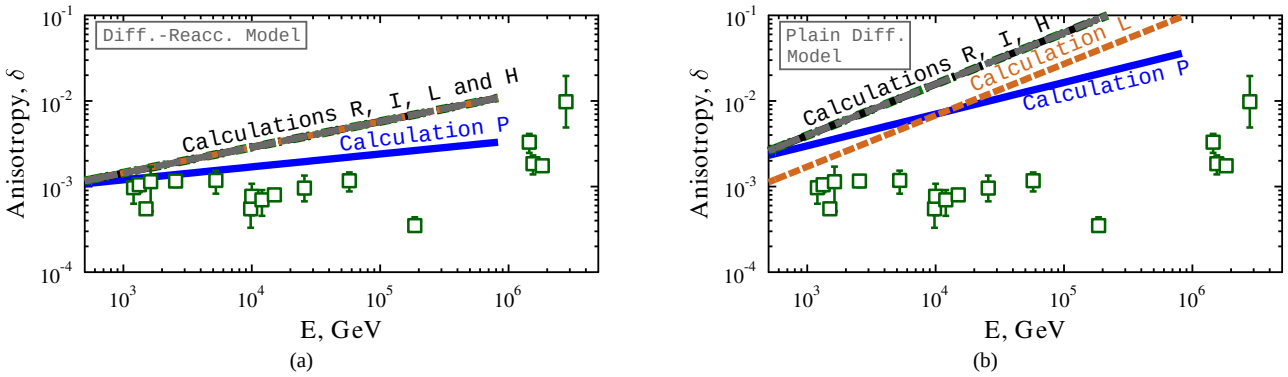

Figure 8. (color in online version) CR flux anisotropy: data from Ptuskin et al. (2006a), together with calculation results. The anisotropy was calculated as the ratio of diffusive flux in the radial direction to the isotropic flux at the corresponding energy. *Left*: diffusive-reacceleration model, *right*: plain diffusion model. *Calculations R, S, I, L* and *H* all predict the same value of anisotropy, and their respective lines overlap. The result of *Calculation P* is different due to a different form of the CR diffusion coefficient. See the discussion in Section 4.3

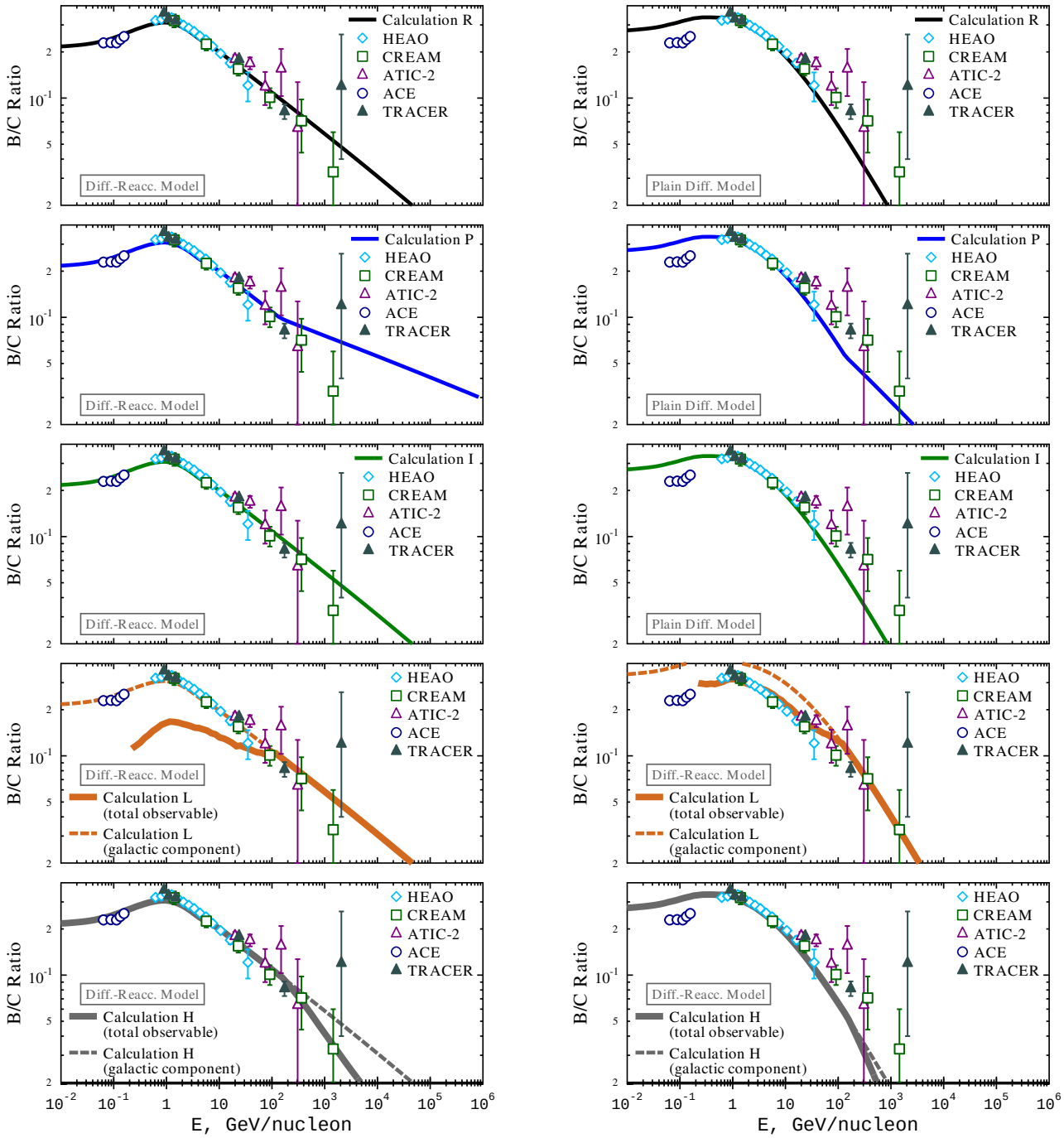

(a) (b)

Figure 9. (color in online version) CR boron-to-carbon flux ratio. *Left*: diffusive-reacceleration model, *right*: plain diffusion model. Data: Davis et al. (2000) (ACE), Engelmann et al. (1990) (HEAO-3), Ahn et al. (2008) (CREAM), Panov et al. (2008) (ATIC-2) and Obermeier et al. (2011) (TRACER). For *Calculation L* and *Calculation H*, dashed lines show the ratio of just the Galactic source, while solid lines show the B/C ratio including the contribution of the "local" source component. Additional discussion in Section 4.4

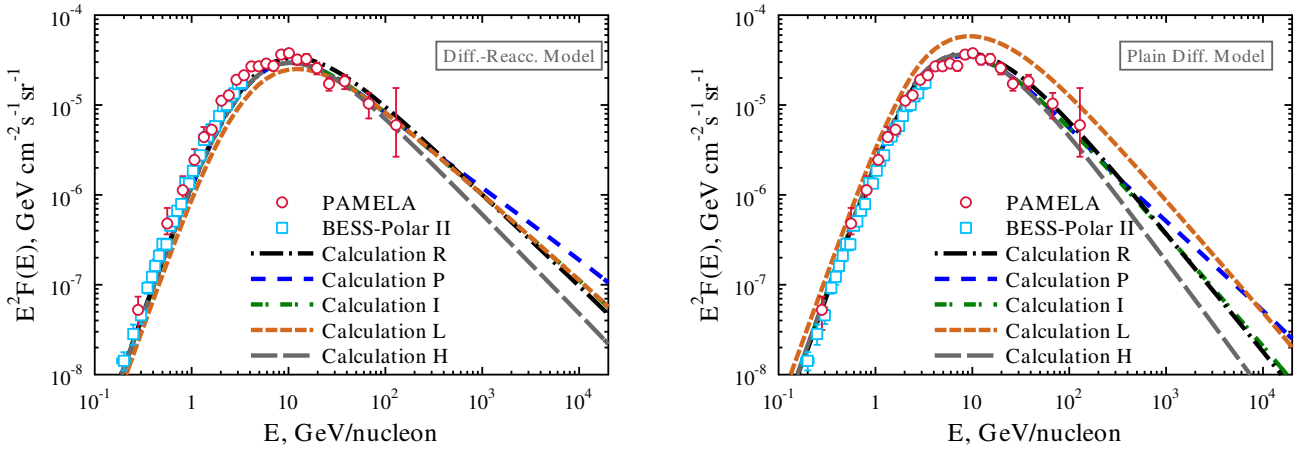

Figure 10. (color in online version) CR antiprotons: data from Adriani et al. (2010) (PAMELA) and Abe et al. (2011) (BESS) together with calculation results. *Left*: diffusive-reacceleration model, *right*: plain diffusion model. See the discussion in Section 4.5

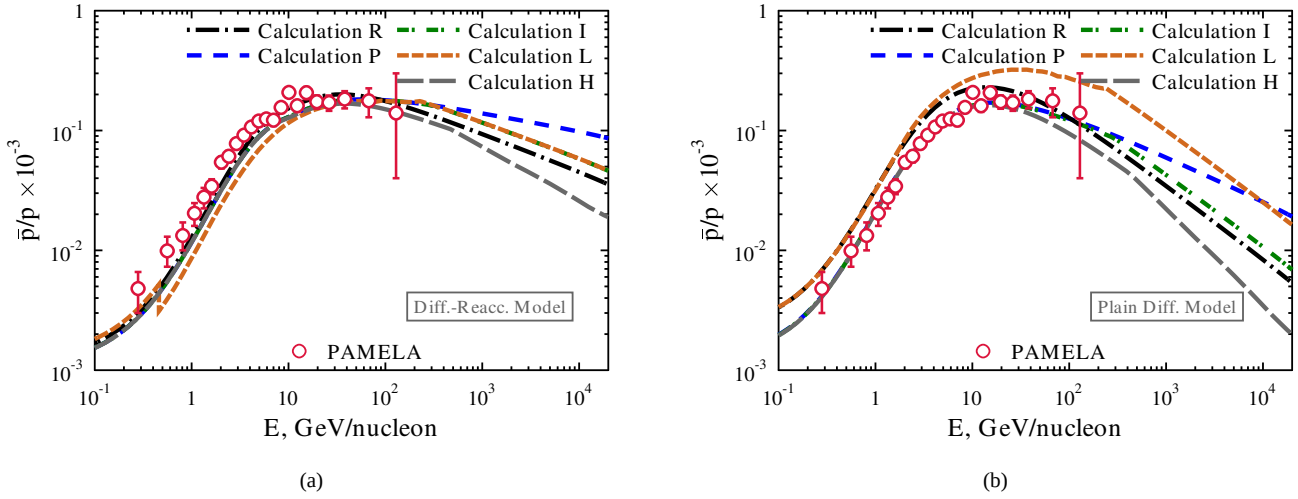

Figure 11. (color in online version) CR antiproton to proton ratio: data from Adriani et al. (2010) (PAMELA) together with calculation results. *Left*: diffusive-reacceleration model, *right*: plain diffusion model. See the discussion in Section 4.5

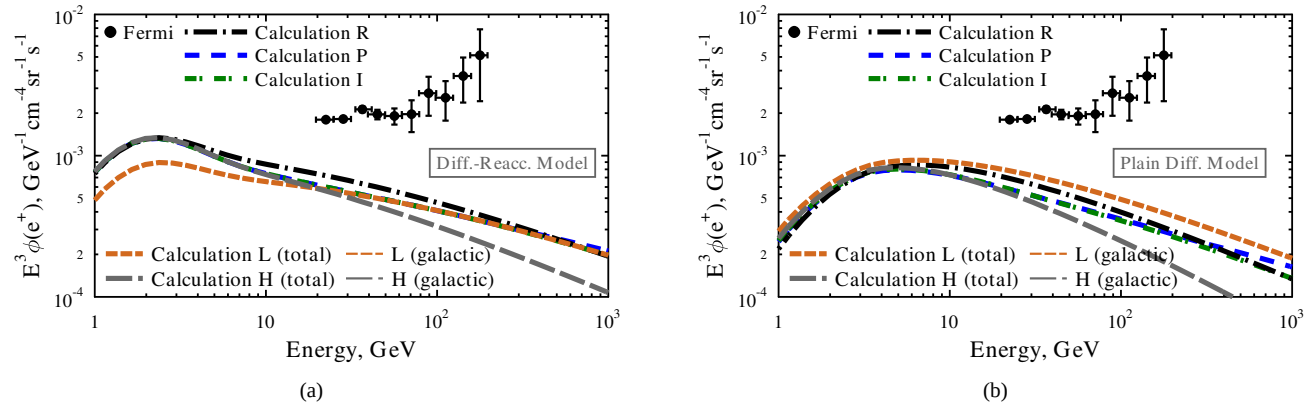

Figure 12. (color in online version) Positron flux: models and data. *Left*: diffusive-reacceleration model, *right*: plain diffusion model. The data are from Ackermann et al. (2012) (*Fermi*-LAT). See the discussion in Section 4.6

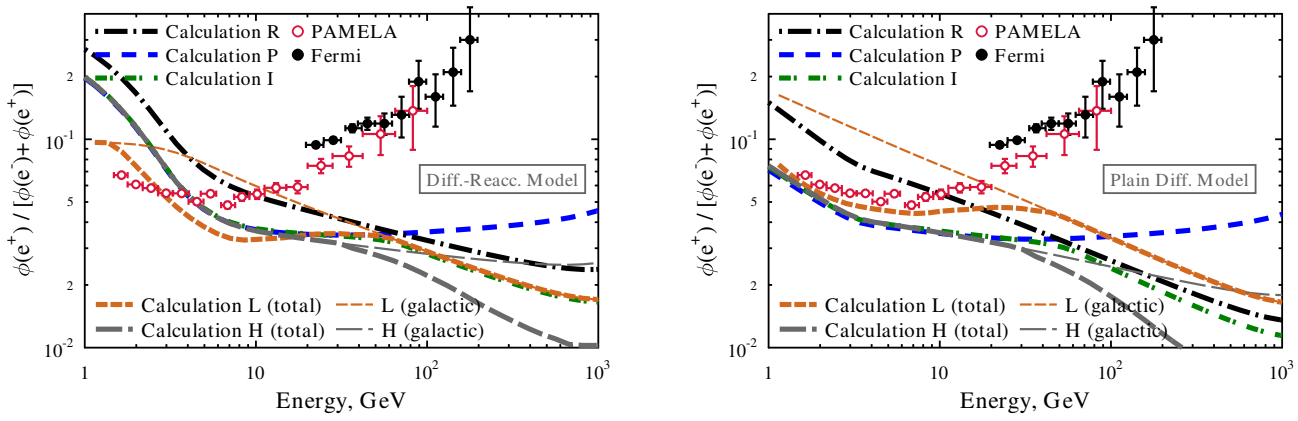

Figure 13. (color in online version) Positron fraction: models and data. *Left*: diffusive-reacceleration model, *right*: plain diffusion model. The data are from Adriani et al. (2009) (PAMELA) and Ackermann et al. (2012) (*Fermi*-LAT). See the discussion in Section 4.6

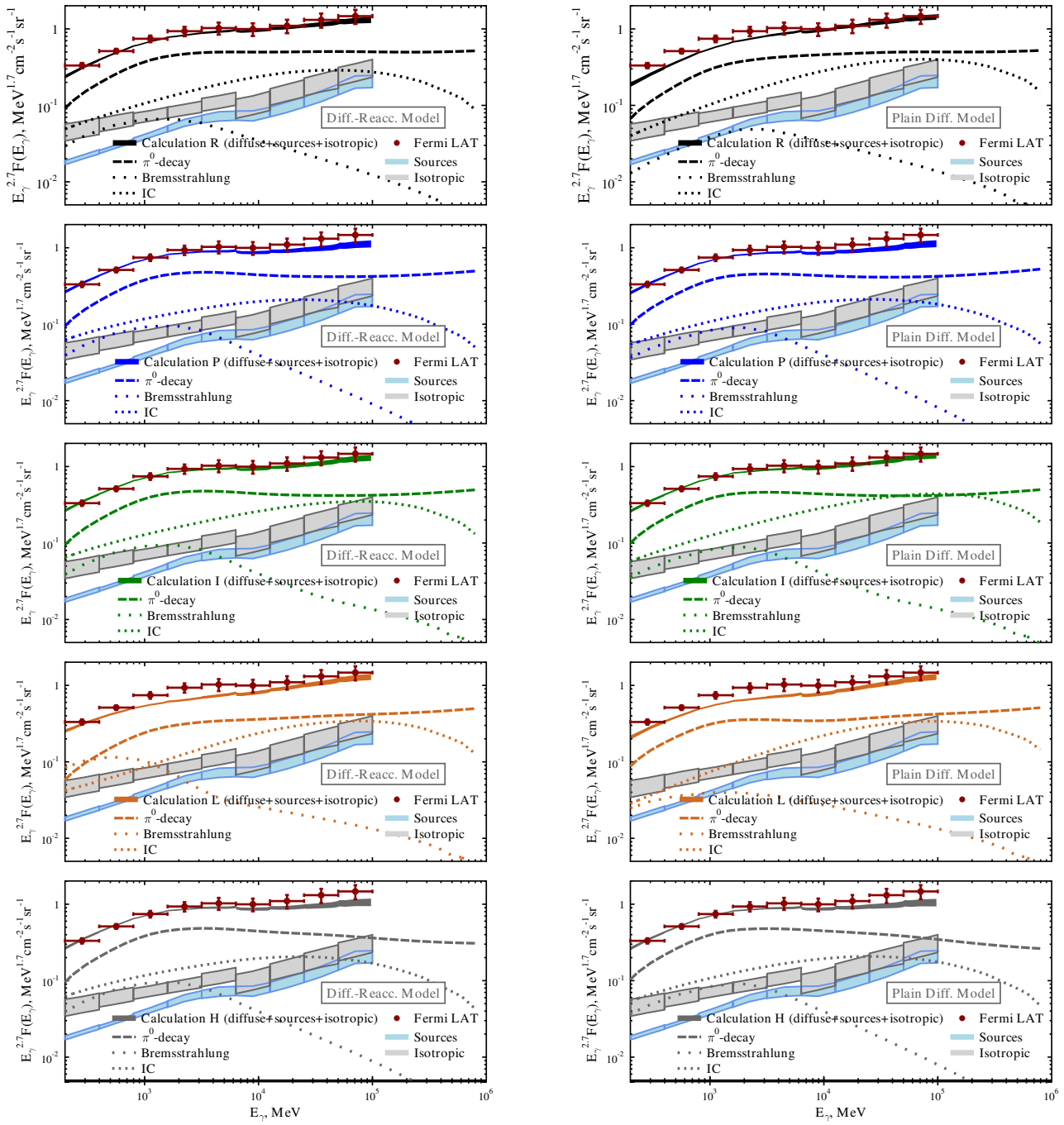

(a) (b)

Figure 14. (color in online version) Diffuse γ-ray emission from intermediate Galactic latitudes: data from Abdo et al. (2010) (*Fermi*-LAT) together with calculation results. *Left*: diffusive-reacceleration model, *right*: plain diffusion model. The data are the diffuse γ-ray intensities averaged over all Galactic longitudes and intermediate Galactic latitudes $10^\circ < |b| < 20^\circ$, as reported by Abdo et al. (2010) (available in the online supplementary material to the article). See the discussion in Section 4.7